Material Dependent Non-linearity and Gain in $SrTiO_3$ Parametric Amplifiers

Masterthesis

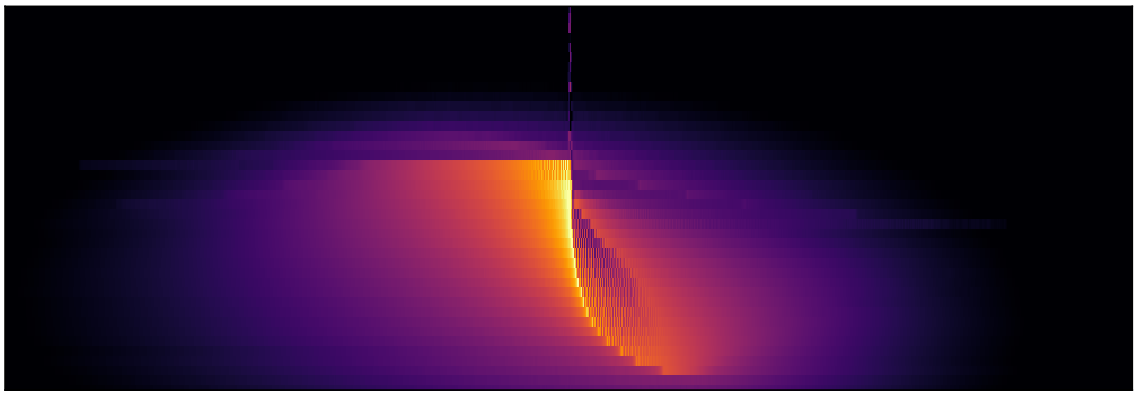

Submitted by:
Karthekan Sivasubramaniam

Supervisors:
Prof. Dominik Zumbühl
Dr. Rafael Eggli

Department of Physics
University of Basel
Switzerland

April 30, 2026

Abstract

Parametric amplifiers are key components for low-noise signal amplification in quantum technologies, allowing the detection of extremely weak signals. Their applications span from quantum optics experiments and the readout of spin-qubits to the search for axionic dark matter. Ideally, such amplifiers should be resilient to magnetic fields, reach the quantum noise limit over a broad frequency range, and maintain a high gain.
In this work, $SrTiO_3$ (STO) based varactors are integrated into a quantum paraelectric parametric amplifier (QPPA) circuit and investigated at cryogenic temperatures. Specifically, the influence of electrode stack configurations, containing gold electrodes with and without chromium or titanium adhesion layers over STO, were systematically investigated on the non-linear dynamics and amplification performance.
The results show that adhesion layers significantly affect capacitance tunability, hysteresis, and achievable gain through interface-induced defects and interdiffusion. Devices without adhesion layers suffer from poor reproducibility, poor amplifier performance and mechanical instability. Although high parametric gain can be achieved, it requires relatively large pump powers, leading to higher-order non-linear effects, increased noise, and dissipation. Furthermore, the amplifier operates stably in magnetic fields up to 5 T, confirming its potential for magnetic-field-compatible applications. These findings highlight the importance of materials and interface engineering for optimizing STO-based parametric amplifiers.

Declaration of Independent Authorship

I attest with my signature that I have completed this paper independently and without any assistance from third parties and that the information concerning the sources used in this paper is true and complete in every respect. All sources that have been quoted or paraphrased have been referenced accordingly. Additionally, I affirm that any text passages written with the help of AI-supported technology are marked as such, including a reference to the AI-supported program used. This paper may be checked for plagiarism and use of AI-supported technology using appropriate software. I understand that unethical conduct may lead to a grade of 1 or "fail" or to expulsion from the course of studies. I have taken note of the fact that in the event of a justified suspicion of the unauthorized or undisclosed use of AI in written performance assessments, I am upon request obligated to cooperate in confirming or ruling out the suspicion, for example by attending an interview.

Karthekan Sivasubramaniam 30.04.2026

AI Usage Statement

I hereby declare that I used ChatGPT throughout this thesis exclusively for linguistic refinement of my own text, including improving clarity, structure, and readability, as well as for assistance in optimizing code for data visualization. The meaning, analysis, and conclusions presented are entirely my own or properly cited.

Contents

1 Introduction

The detection of weak signals is a fundamental requirement across a wide range of physical systems, from long-distance space communication [1] or gravitational wave detection [2], to sensing the tiniest light axion-like particles, to even confirm the existence of dark matter [3]. In many modern experiments, the signal of interest is intrinsically small and often degraded by noise, imposing strict requirements on the sensitivity of the measurement chain.

As an example, minute signals at radio frequencies are used to detect fragile qubit states in semiconductor quantum dots (QDs), which are a promising platform for quantum computation. QDs are quantum bits (qubits) operating at cryogenic temperatures. What makes them advantageous to a regular bit is the ability to exhibit superposition and entanglement [4, 5]. Furthermore, they are very scalable due to similar fabrication to classical transistors [6].

One key requirement for realising a functional quantum computer is the high-fidelity readout of the qubit state. Consequently, the QD needs to maintain a stable spin-state at 4 K or below during measurement [7]. A major challenge in this context is to extract maximum information from a naturally weak signal that is further diminished by external noise. To reliably detect such weak signals, an amplifier is required that delivers high gain, exhibits extremely low noise, supports a broad bandwidth, shows minimal fluctuation-dissipation, and is resistant to magnetic fields, as the qubit is operated in their presence [7]. Under these conditions, the amplifier can maximise the signal-to-noise ratio across a wide frequency range [8].

Commonly, superconducting amplifiers are used because they provide super-low noise performance, but they suffer from a very limited frequency range of operation, limited power handling, and sensitivity to magnetic fields. Semiconductor amplifiers represent an alternative, offering a much broader frequency range, though at the cost of increased noise and significantly higher power dissipation [8–11]. A promising approach to overcome this trade-off is the use of a parametric amplifier, which demonstrates the potential for reduced power dissipation [8]. In such devices, the signal is amplified by modulating an internal parameter with an external pump. This allows transferring energy from the pump to the signal, producing gain [10, 12–14]. This approach not only addresses the key challenges of achieving large bandwidth, high power handling, and resilience against magnetic fields, but also is phase sensitive, and in theory, can reach the standard quantum noise limit [11, 15].

Building on the concept of parametric amplification based on variable capacitance, this work presents a quantum paraelectric parametric amplifier (QPPA) based on a strontium titanate (STO) varactor. This thesis is motivated by earlier efforts on quantum capacitance parametric amplifiers[8], which inspired the study of [16]. Later works expanded on similar device concepts and realizations [16, 17], providing the foundation for the ongoing investigation reported in this study.

This work first presents the theoretical foundations of parametric amplifiers, including their behaviour and the role of STO in making the system paraelectric, which leads to the QPPA. It then briefly discusses the material properties relevant for fabricating the varactors. Next, the device and circuit models are introduced. Then, the device performance in both reflection and transmission modes is analysed, and a systematic comparison of different electrode stacks is provided. In addition, magnetic field dependence and anomalies are examined. Finally, a conclusion and an outlook are presented.

2 Theoretical Background

2.1 Parametric Amplification

Parametric amplification (PA) is a non-linear mechanism, in which energy is transferred between different frequency components of a system through time dependent modulation of one of its intrinsic parameters, such as the inductance or capacitance of a resonant tank circuit [10, 12–14].
In electrical resonators, such as an LC circuit, this mechanism can be realised by introducing a non-linear reactive element whose properties depend on the applied DC voltage [10]. In our QPPA this element is an STO varactor. At cryogenic temperatures, STO exhibits a strongly non-linear dielectric response to an external DC bias, enabling parametric interactions between a pump and signal tone [18, 19].
The origin of these interactions can be understood from the non-linear polarisation response of the medium. Since the capacitance is directly related to the dielectric constant, the polarisation can be expressed as a Taylor expansion of the electric field E as [16, 20]:

$$P(E) = \epsilon_0(\chi^{(1)}E + \chi^{(2)}E^2 + \chi^{(3)}E^3 + ...) \tag{1}$$

Here ϵ_0 represents the vacuum permittivity and χ the susceptibility. Each term in this expansion corresponds to a different order of non-linear interaction. Especially, the second-order term $\chi^{(2)}$ is of interest, as it enables three-wave mixing (Fig. 1). This is one of the fundamental principles of a parametric amplifier. Here a strong pump tone with frequency ω_p couples to a weaker signal tone ω_s and creates an idler tone ω_i, satisfying the energy conservation condition [20]:

$$\omega_p = \omega_s + \omega_i \tag{2}$$

Specifically, this interaction represents a parametric frequency down conversion of the pump tone, where its energy is transferred to the signal and idler tones. The generated idler frequency satisfies:

$$\omega_i = \omega_p - \omega_s, \tag{3}$$

which corresponds to difference-frequency generation (DFG). This process can be differentiated into the degenerate and non-degenerate case. In the degenerate case, where $\omega_s = \omega_i = \omega_p/2$,

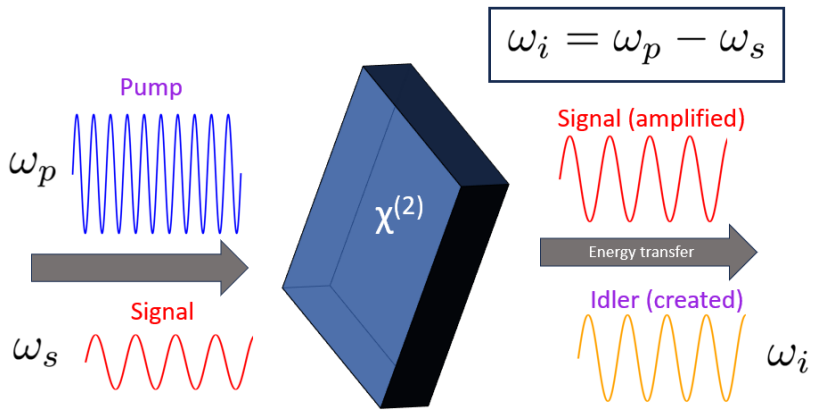

Figure 1: **Three-wave mixing.** A strong pump (ω_p) and weaker signal (ω_s) tone interact in a non-linear ($\chi^{(2)}$) medium to generate an idler at $\omega_i = \omega_p - \omega_s$, transferring energy from the pump to the signal and idler.

the amplification becomes phase-sensitive, due to interference. Thus, the gain depends on the relative phase ϕ between the pump and signal fields and can be expressed as

$$G(\phi) = G_0 \cos(\phi), \tag{4}$$

where G_0 denotes the maximum achievable gain. Depending on the relative phase difference, the signal can either be amplified or attenuated. For the non-degenerate case the gain is phase-insensitive.
In practice, there are different definitions of gain. The *parametric gain* refers to the increase of the signal amplitude due to the pump. The *effective gain* additionally accounts for system losses and imperfections [21]. An example is given in Tab. 1.

	Parametric Gain	Effective Gain
Signal Input (1)	-40 dBm	-40 dBm
Amplified Signal Output (2)	-10 dBm	-10 dBm
Total Loses (3)	5 dBm	5 dBm
Gain	35 dB (2-1+3)	30 dB (2-1)

Table 1: Example showing the difference between parametric and effective gain.

2.2 Duffing Non-Linearity

This section follows the discussion of Duffing non-linearity in [22, 23].
An ideal parametric amplifier reaches unlimited exponential growth via three-wave mixing in the absence of sufficient damping. In practice, however, higher-order non-linear (HONL) terms limit and stabilise the amplitude.
In the low-power regime, the second-order term $\chi^{(2)}$ gives a good description of an ideal parametric amplification process, whereas for higher pump powers, HONL become more dominant. In particular, the third-order term $\chi^{(3)}$ gives rise to additional effects commonly known as Duffing non-linearity. To describe the dynamical behaviour of the resonator, it is helpful to map the LC circuit to an harmonic oscillator model. In this analogy, the charge in the circuit corresponds to the displacement of a mechanical oscillator, while the non-linear capacitance translates into a non-linear restoring force. As a result, considering HONL, Newton's equation of motion can be extended by adding a cubic term:

$$\ddot{x} + \omega_0^2 x + \beta_3 x^3 + \Gamma \dot{x} = \frac{F_0}{m} \cos(\omega t), \tag{5}$$

where ω_0 is the resonance frequency, β_3 the Duffing non-linearity coefficient, Γ the damping rate, F_0 the external driving force and m the effective mass of the resonator.
Using the Krylov-Bogolyubov averaging method the amplifier behaviour can be described by slowly varying quadratures u and v in the rotating frame at a drive frequency ω[24–26]. The first - order averaged solution is[1]:

$$\dot{u} = -\frac{u\Gamma}{2} - \frac{3u^2 v\beta_3}{8\omega} - \frac{3v^3\beta_3}{8\omega} + \frac{v(\omega^2 - \omega_0^2)}{2\omega} + \frac{F_0 \sin(\theta)}{2m\omega}, \tag{6}$$

$$\dot{v} = -\frac{v\Gamma}{2} v + \frac{3v^2 u\beta_3}{8\omega} + \frac{3u^3\beta_3}{8\omega} - \frac{u(\omega^2 - \omega_0^2)}{2\omega} - \frac{F_0 \cos(\theta)}{2m\omega}. \tag{7}$$

[1]For the detailed derivation, see [23].

By numerically solving for the steady-state solution ($\dot{u} = \dot{v} = 0$) of Eq. 6,7 one obtains the oscillating amplitude X(ω) given by:

$$X(\omega) = \sqrt{u^2 + v^2}. \tag{8}$$

Fig. 2 shows the oscillating amplitude X(ω) as function of the drive frequency ω for different values of β_3 = -50 (1), -1000 (2), and -4000 (3). The response shows a strong dependence on β_3. For a positive Duffing coefficient ($\beta_3 > 0$), the X(ω) bends towards higher frequencies, while for negative β_3, it bends toward lower frequencies.
Below a threshold value of β_3 the amplifier response shows a single stable solution. As β_3 increases beyond this threshold the response becomes bistable, meaning two stable solutions exist. The stable solutions are indicated by solid lines and the unstable solutions are indicated by dotted lines. The point at which the solid and dotted line merge, represents bifurcation points, which define the initiation of instability.
In regards to the parametric amplifier, the Duffing non-linearity does not directly contribute to the amplification mechanism, but alters the performance and stability for high pump powers. Its main impact is to introduce an amplitude dependent resonance frequency shift, which can alter the parametric condition $\omega_p = \omega_s + \omega_i$, hence the resonance frequency has to be chosen as a function of the pump power to optimize gain. Therefore controlling and understanding the Duffing non-linearity is desired to optimize the amplifier performance.

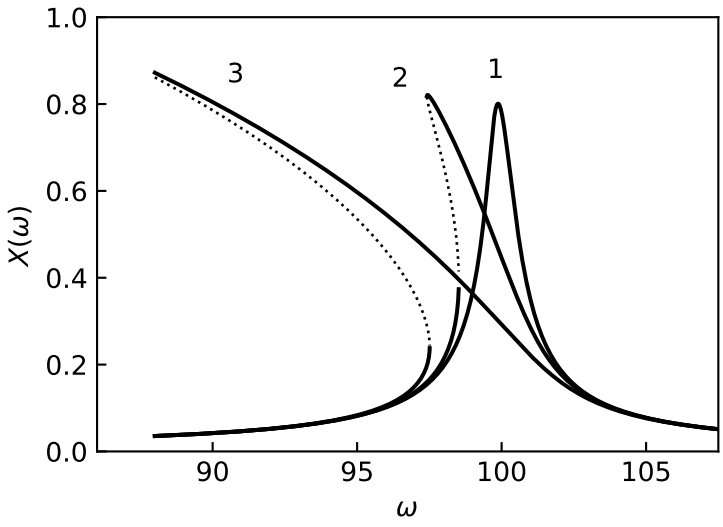

Figure 2: The steady-state solution of a Duffing resonator (Eq. 6,7) in the rotating frame is calculated for m = 1, $\omega = 100$, $\Gamma = 1$, $F_0 = 80$ and $\theta = 0$. Trace **(1)** corresponds to β_3 = -50, **(2)** to β_3 = -1000, and **(3)** to β = -4000. The dotted lines indicate the unstable branches. Fig. replicated and adapted from [23].

2.3 Non-Linear Damping

The following section builds on the discussion presented in [14, 23].
Damping has a significant impact on PA because it directly affects the resonators dissipation response. A differentiation can be made between linear and non-linear damping. Linear damping can be understood as the competition between intrinsic losses and the parametric pump. As the pump power increases, the effective damping decreases. When the damping approaches zero the QPPA transitions into a region of instability and self-oscillates, even in the absence of

a driving force [14, 27].
In reality, however, damping becomes non-linear (NL) for large enough amplitudes. This can be integrated into Newton's equation of motion, by extending the damping term. In the model described in [14], the damping takes the form

$$2(\Gamma_1 + \Gamma_2 x^2)\dot{x} \tag{9}$$

where Γ_1 is the linear and Γ_2 the NL damping coefficient. Applying averaging methods leads to quadrature equations, where the presence of $\Gamma_2 > 0$ increasingly suppresses the growth of the oscillation amplitude. As a result, both the achievable gain and oscillation amplitude are limited. [14].
In addition, NL damping interacts with the Duffing non-linearity and further modifies the QPPA response. In particular, for large drive amplitudes, if the NL damping is large enough, the Duffing bistability can be suppressed. As a consequence, the QPPA response can transition between different topologies (Fig. 3). For example, in the presence of a Duffing non-linearity bigger than zero, the amplitude bends horizontally (Fig. 2, 3c). At higher pump powers more complex structures such as isola (Fig. 3b,c)[2] and/or double peaks with loops inbetween can emerge (Fig. 3e,f). For a in-depth derivation and insight into the underlying mathematics, see [14].

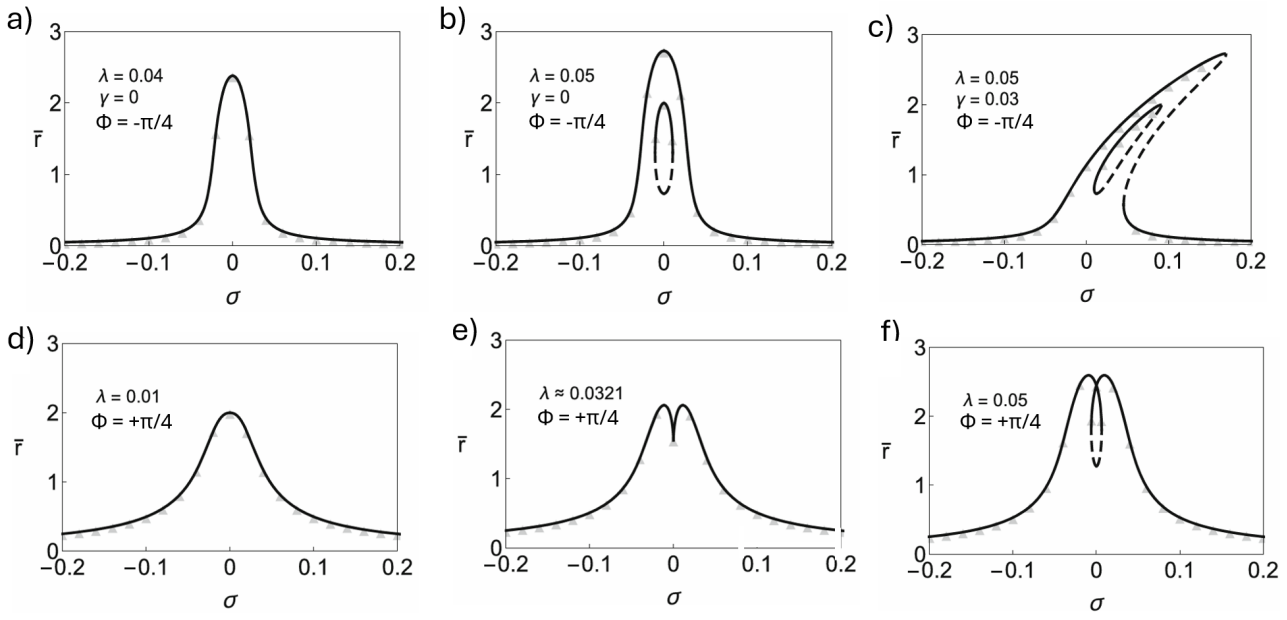

Figure 3: Frequency response as a function of the tuning parameter σ for different pump levels λ. The tuning parameter $\sigma = 3\gamma\bar{r}^2/4\omega_0^2$ describes the amplitude dependent frequency shift, where γ represents the non-linear Duffing term, ω_0^2 the resonance frequency and $\bar{r}$ the steady-state amplitude. In **a), b)** the Duffing non-linearity γ is set to zero (no bending) and for increasing pumping an isola emerges. In **c)** analogous to b) but with $\gamma = 0.03$, bending occurs. In **d), e), f)** the Duffing NL is $\gamma = 0$, where increasing pumping leads to double peaks and loops. The relative phase is set to $\phi = -\pi/4$ in **a), b), c)** (minimal gain) and $\phi = +\pi/4$ in **d), e), f)** (maximal gain). For a relative phase $-\pi/4 \leq \phi \leq +\pi/4$ the isola and loops can be off-centred. Figures adapted from [14].

Overall, it is better to handle damping in PA as an amplitude dependent term rather than a fixed dissipation value. Linear damping sets the threshold for where the parametric instability starts, whereas the NL damping controls how the QPPA saturates and stays stable

[2]These isola were observed experimentally already in [28, 29].

at higher pump levels and amplitudes. Together with the Duffing NL, this gives a more advanced description of parametric amplifier dynamics, especially at higher pump powers.

2.4 1 dB Compression Point

Previously, it was discussed that non-linear terms can have a significant influence on the behaviour of a parametric amplifier. A common way to investigate the onset of non-linearity is illustrated in Fig. 4. It presents the signal output power P_{out} as a function of the signal input power P_{in}. This is an important plot used to characterise the non-linear behaviour of RF amplifiers. In the ideal linear regime, at low P_{in}, an amplifier provides a constant gain such that the output power increases linearly with the input power (slope = 1). For example, an amplifier with a gain of 10 dB produces an output power of 11 dBm for an input power of 1 dBm.
In reality, amplifiers deviate from this ideal linear behaviour when the input power becomes sufficiently large. As the input signal increases, physical limitations of the device cause the gain to decrease and the amplifier enters the compression regime [30–33].

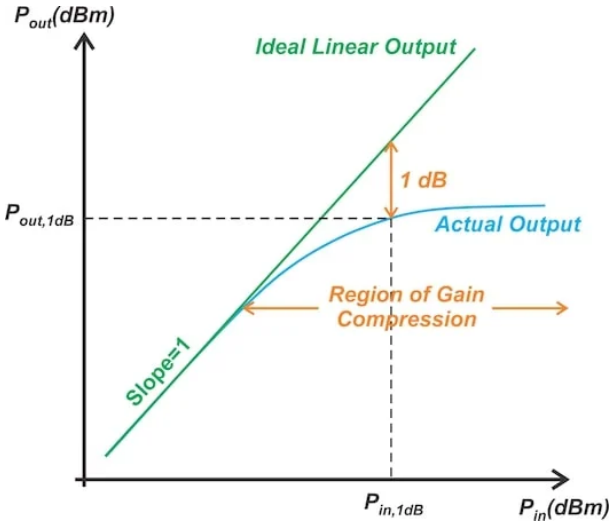

Figure 4: The signal output power P_{out} as a function of the signal input power P_{in} is shown for an RF amplifier. In the low input power regime, the P_{out} is linear. As P_{in} increases, P_{out} starts to deviate from the ideal linear output, which is the onset of the gain compression region. The point where the P_{out} deviates 1 dB from the ideal linear output is called the 1 dB compression point [31].

The 1 dB compression point is defined as the output power at which the actual output is 1 dB below the ideal linear output of the amplifier (Fig. 4). This deviation is an indicator for the beginning of significant non-linear behaviour. The compression point can be defined with respect to the input power ($P_{\mathrm{in,1dB}}$) or the output power ($P_{\mathrm{out,1dB}}$), which are related through the amplifier gain G according to [30, 31]

$$P_{out,dB} = P_{in,dB} + G - 1\,dB. \tag{10}$$

The physical origin of gain compression comes from the non-linear characteristics of the amplifier. For small signal powers, the linear term dominates the process. At higher signal powers, non-linear terms become significant (damping, higher-order terms and intermodulation). As P_{sig} continues to increase, the amplifier eventually approaches its saturated P_{out}, where it no longer increases significantly with increasing P_{sig} [14, 30, 32, 33].

2.5 V_{var} vs P_p Correlation on Gain

Fig. 5 schematically visualises the operating principle by which the QPPA generates gain. The red curve represents the simulated varactor capacitance voltage (C-V) characteristics, calculated using Eq.11. By applying a DC bias, the operating point can be positioned at a desired location along the curve. When a pump tone with pump power P_p is applied, the varactor capacitance oscillates around the chosen DC bias point. For example, with zero DC bias and a pump power of $P_p = 10\,dBm$, corresponding to approximately $2\,V_{pp}$ (peak to peak voltage), the voltage swings symmetrically between -1 V and 1 V. As a result, the capacitance travels both the positive and negative bias regions, which significantly reduces the achievable gain, as the nonlinearity is effectively averaged over regions with different curvature.
In contrast, when a DC bias of 1 V is applied with the same P_p , the voltage oscillation becomes asymmetric and remains in the positive bias region. In this regime, the capacitance tunability between 0 to 1 V is much larger than between 1 to 2 V for the same voltage swing, due to different slopes. This asymmetry impacts the modulation of the capacitance and thus the effective average resonance frequency of the QPPA.
For a fixed DC bias, increasing the pump power P_p leads to a larger capacitance modulation and therefore higher gain, up to the point where the oscillation extends into the negative bias region, or the region with a small slope dominates the C modulation, because the gain degrades due to symmetric averaging effects. Therefore, most optimal PA is achieved if the capacitance oscillation is big within a small voltage range and stays in the positive bias region.

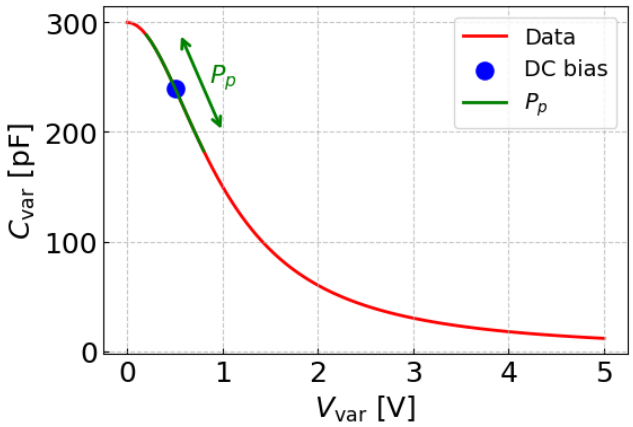

Figure 5: The varactor capacitance is calculated with Eq.11 and is shown in red as a function of applied voltage. The blue dot indicates the applied DC bias, which defines the operating position along the C-V curve. A pump tone with power P_p , illustrated in green, is applied. As the pump power P_p increases, the amplitude of the voltage oscillation grows, resulting in an expansion of the capacitance modulation range around the bias point.

2.6 Materials overview

In this work, the devices are fabricated from multilayer structures consisting of strontium titanate ($SrTiO_3$, abbreviated as STO), gold (Au), titanium (Ti), and chromium (Cr). Each element has distinct physical and electronic properties under cryogenic temperatures, which have a big impact on the overall device performance. Since the goal of this thesis is to investigate the effect of the materials on the device performance, it is essential to understand how these materials behave individually and especially in combination at temperatures around 4 K or below. Also, because all films are fabricated in the nanometer thickness regime, their electrical, structural, and dielectric characteristics can be very different from those of bulk materials

[19]. Such variations are strongly dependent on growth parameters including film thickness, deposition rate, oxidation level, substrate temperature, surface adsorption, grain boundaries, roughness and defects, all of which can substantially alter the final electronic and dielectric behaviour [34, 35]. This chapter provides an overview of the relevant properties of the elements used to fabricate the devices, particularly those that may affect the non-linear dielectric properties of the QPPA.

2.6.1 Strontium Titanate

Strontium Titanate (STO) is a versatile perovskite oxide (ABO_3 structure) widely studied for its wide range of structural, electrical, magnetic, thermoelectric, and quantum properties [36–38]. At room temperature, STO behaves as an insulator with a cubic structure (Fig. 6a). Its lattice constant is 3.9 Å [39]. It shows no ferroelectricity and has a bandgap of 3.15 eV (Fig. 6b). Upon cooling, it undergoes a structural phase transition from the cubic to a tetragonal phase at ≈ 100-110 K [19, 37, 40]. Around ≈ 65 K it transitions to orthorhombic [18].

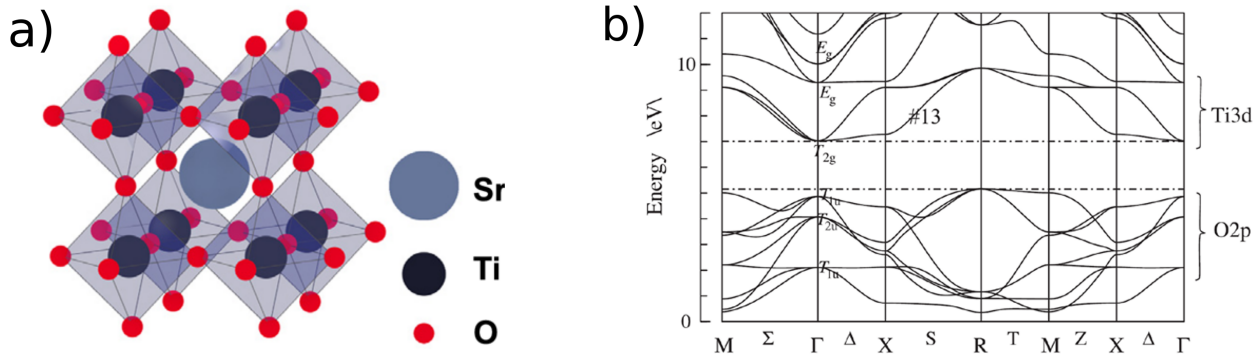

Figure 6: **a)** STO cubic structure with Sr at the cube corners, Ti at the body centre, and O at face-centres is shown for room temperature.

As temperatures decrease below the Curie temperature T_c, usually a ferroelectric phase transition characterized by a saturating dielectric constant (Fig. 7b) and phonon mode frequency decrease to zero is observed (see Fig. 7a). For STO however at low temperature it gets very close to a ferroelectric phase transition, but quantum fluctuation prevent the formation of ferroelectric ordering, making it a quantum paraelectric material [19, 36, 37, 40–42]. Consequently, STO exhibits a very large dielectric constant ϵ that increases strongly with decreasing temperature and decreases under increasing DC bias, as experimentally determined in [18] and shown in Fig. 7c). At 4 K, where STO is close to transitioning to ferroelectric, the dielectric constant saturates to $\epsilon_r \approx 30'000$. [19, 36, 37, 41, 43–45]. Under mechanical strain STO can become ferroelectric and for chemical doping it can become a metal or superconductor [46].

The combination of quantum fluctuations and highly non-linear dielectric tunability makes STO a very interesting material at low temperatures, with high potential for being used in a broad spectrum of applications. Its remarkable dielectric properties, tunable polarisation, and potential superconductivity establish STO as a popular system in modern condensed matter physics. Consequently, STO serves as an active platform for studying arising quantum phenomena [47].

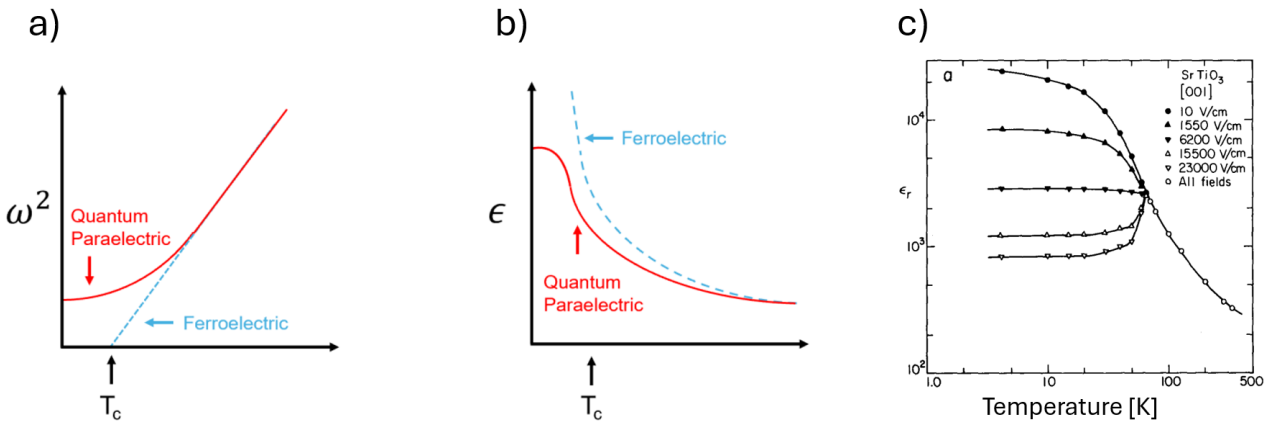

Figure 7: **a**) Temperature dependence of the phonon mode is shown. T_C denotes the transition temperature, where the phonon mode of ferroelectric (blue) state decreases to zero or is aborted for quantum paraelectric (red) state. **b**) Temperature dependence of the dielectric constant, which saturates for quantum paraelectric and diverges for ferroelectric at T_C [41]. **c)** The relative permittivity as function of temperature and DC bias is shown for STO (orientation [001]) for different DC biases. Figure adapted from [18].

In this work, STO is used as a varactor. Its capacitance as a function of applied DC voltage, at temperatures below 10 K, can be approximated by Johnson's relation [45, 48, 49]

$$C_{\mathrm{var}}(V_{\mathrm{var}}) = \frac{C_0}{\left(1 + \frac{(V_{\mathrm{var}} - V_{\mathrm{offset}})^2}{V_0^2}\right)^{1/3}} \tag{11}$$

Here, V_{var} denotes the electric field applied to the varactor, C_0 is the capacitance at zero field, and V_{offset} corresponds to the experimentally observed shift of the maximum capacitance relative to V_0. This tunable capacitance serves as the variable element in an LC resonator used for parametric amplification. Such an approach could potentially be very attractive in applications that require low-noise amplification and insensitivity to magnetic fields.[8, 49].

2.6.2 STO - Hysteresis and Defects

Hysteresis in the dielectric constant of STO appears at cryogenic temperatures when it experienced an external bias voltage. Consequently, the capacitance tunability depends on the history of the applied electric field, which creates a hysteretic loop-like behaviour in capacitance-voltage characteristics [45, 49–51]. The cause for this hysteresis is explained with trapped charges, which reduce the number of conducting electrons in STO. The microscopic origin is still unclear [51]. One proposed mechanism includes trapping of electrons via clustered oxygen vacancies induced by an applied electric field [45, 49, 52]. The number of trapped charges is strongly impacted by the extrinsic defects such as oxygen vacancies, doping and impurities created during substrate preparation, interface defects [53] or crystal growth [45, 52]. These defects generate internal electric fields, reducing the quantum paraelectricity of STO.
In addition, STO itself can provide intrinsic charge trapping sites. At ≈ 105 K, STO transitions from cubic to tetragonal [19, 37, 40], creating regions within the crystal, called domains, where the lattice distorts in different directions. The boundaries between these domains are called domain walls. Due to strain gradients and lattice coupling in the tetragonal phase transition these walls become intrinsically polar [54–57]. This local polarity of the domain walls can act as charge trapping sites and contribute to the reduced conduction electrons due to domain wall

pinning [45, 51, 58]. The history dependence can be reset by thermally reheating STO to room temperature [45, 49–51].

2.7 Dielectric losses

This chapter addresses the main loss mechanisms in a tunable paraelectric varactor in response to microwave (MW) signals. In an ideal, defectless, single crystal paraelectric, losses are minimal and arise only from intrinsic defects, characterised by the material's minimum loss tangent (see chapter 3.1) [59].
These intrinsic losses mainly result from the interactions between MW fields and phonons [59]. In this process, MW energy is absorbed by the crystal's thermal phonons and dissipated as heat. The absorption mainly occurs through three-wave mixing. Additional intrinsic losses may occur under external fields, for example, a DC bias that breaks the crystal lattice symmetry or high-power microwave excitation, both of which can promote microwave-to-acoustic phonon conversion through electrostriction and the inverse piezoelectric effect. In thin-film crystals, further attenuation may occur at material interfaces , such as adhesion layers or electrodes [59].
In real crystals, extrinsic defects, most notably oxygen vacancies, often represent the dominant source of loss. These defects can be uniformly distributed in bulk STO thin film or concentrated at the interface, where they create local electric fields, activating both electrostrictive and converse piezoelectric effects. Consequently, MW energy is converted into acoustic waves originating from these defect sites. These acoustic waves propagate through the crystal, carrying away energy from the electromagnetic field and thereby attenuating the microwave signal [59].
In high-quality crystals, intrinsic and extrinsic losses become comparable, with intrinsic mechanisms potentially dominating [59]. In this work, single-crystal STO [001] was investigated using radio-frequency (RF) signals. Although the energy ($E = hf$) of RF radiation is significantly lower than that of microwave excitation, the STO samples may exhibit similar loss behaviour for very strong pumping. This observation suggests that the density of extrinsic defects in the investigated crystals is sufficiently high and dominates the loss mechanisms.

2.8 Gold - Electrode

Gold is among the most chemically stable elements. Its resistance to corrosion and environmental degradation is one of its most desired properties. Its high chemical stability is strongly associated to its ionization potential (9.2 eV), making the metal largely resistant to oxidation and oxygen absorption at room temperature. Therefore Au is widely used in electronic devices, where long-term integrity is required. [60–62].
When the thickness of Au films is reduced from bulk to nanometer scale, the electrical resistivity ρ linearly increases. Precise control over the film thickness is therefore very important to consistently reproduce identical layers. Differing layer thicknesses can affect the surface roughness and activate the surface area, which will influence the device performance [63]. If the thickness is reduced to below 10 nm it transitions from metal to insulator [64].
The increase in resistivity is explained with increased electron scattering due to surface interactions, adsorption processes, impurities, grain boundaries, and film surfaces[63, 65].
In addition to electrical properties, surface morphology of Au plays a crucial role in determining its chemical reactivity. Experimental studies have revealed a clear correlation between surface roughness and surface interactions [61, 62]. Specifically, depositing gold nanoparticles onto an otherwise smooth Au surface has been shown to increase its chemical reactivity. While oxygen

molecules do not adsorb on flat Au(111) surfaces, they do bind to Au clusters on rough Au surfaces. This enhanced roughness is accompanied by a reduction in workfunction (WF) from 5.18 to 3.942, as calculated via density functional theory, indicating that surface roughness has a strong impact on the WF, which is a fundamental material parameter controlling surface chemical processes. These findings demonstrate that surface morphology has a significant impact on the electronic and chemical behaviour of Au [61, 62].

For 70 nm thick Au films a resistivity of 5 nΩ·m was measured at 4 K [66]. This low ρ makes Au a highly efficient conductor with low self heating and energy dissipation, very suitable for capacitor electrodes integrated on STO for low voltage applications or other electronic nano devices [67, 68].
Despite its excellent electrical conductivity and chemical stability, Au is generally avoided in complementary metal-oxide-semiconductor (CMOS) due to its destructive diffusion, contamination and alloy properties [69–71]. It also exhibits high interdiffusivity into dielectric resonators such as silicon and germanium [70, 72], or other metals like copper[71], aluminium [73] or Cr and Ti [74]. As a consequence the interface defects and electric resistivity are often increased due to formation of deep-level trap states within the bandgap, severely degrading carrier lifetime and device reliability. [75, 76]. Therefore, understanding what happens at the interface between Au and STO is very important for specific application.
It was experimentally observed, that near and at Au/STO(001) interfaces the formation of oxygen vacancies is significantly promoted and thermodynamically migrated to the interface [38]. This could potentially shield STO from being efficiently polarised, hence capacitance tunability reduced, when DC biasing the Au electrodes. Additionally if ion beam is used in the fabrication process it is reported to enhance Au interdiffusion even more [76]. This interdiffusion increases interface defects and resistivity [76]. On top of all of that, Au has drawbacks like delamination, peeling[3] and time dependent device performance [74]. To tackle interdiffusion and peeling, diffusion barriers or adhesion layers can be utilised, which may significantly influence the electrical properties of the device. In this work,y Cr and Ti adhesion layers between STO and Au are used and investigated.

2.9 Chromium And Titanium - Adhesionlayer

Cr and Ti are transition metals very commonly used as adhesion layer for Au thin films on dielectric substrates. Their higher chemical reactivity compared to Au enables strong bonding to the underlying substrate [74]. By contrast, when pure Au is deposited directly on a dielectric, it exhibits poor spreading, forming discontinuous films at small thicknesses and rough, continuous films only at larger thicknesses (around 20 nm) [74].
Adding a Ti or Cr adhesion layer significantly modifies film growth dynamics. Both metals improve Au spreading, which raises the nucleation density, and leads to smaller grains with a narrower size distribution. As a result, Au films become smoother [74]. In Ti/Au systems, a thin Ti layer (2 nm) enables continuous Au growth and affects the grain size and texture. The Ti layer is typically amorphous due to partial oxidation that enhances adhesion, whereas the Au overlayer remains crystalline. At room temperature, no significant Ti/Au interdiffusion is detected [74].
For Cr/Au films, similar surface improvements are seen compared to Ti/Au. However, Cr and Au undergo pronounced interdiffusion. Particularly in thinner films, partial alloy formation is more prominent [74].
These adhesion layers also affect the electrical properties. In polycrystalline thin films reduced

[3]Peeling is very bad, when wire-bonding onto Au and it does not stick due to insufficient adhesion.

conductivity is observed due to surface and grain-boundary scattering. Nevertheless, Ti/Au films have a lower sheet resistance than pure Au, which is credited to an effectively increased conducting thickness. In contrast, Cr/Au exhibit interdiffusion, resulting in the alloy having increased resistance [74].
The interactions between STO and the various materials are poorly characterised, even though they would be among the most interesting aspects to study. What can be said is that STO contains oxygen and titanium, which are very likely to interact with the adhesion layers. As more defects are introduced into STO, its dielectric behaviour becomes increasingly difficult to predict theoretically, because STO is an extremely versatile material that exhibits a wide range of properties when doped.

3 Device

This chapter presents the device and circuit implementation of the quantum parametric amplifier (QPPA) used in this work. It first introduces the theoretical circuit model in the ideal case and then discusses deviations arising from non-ideal effects such as parasitic elements and material losses. Then the dielectric loss mechanisms are described through the loss tangent. Finally, the practical realisation of the device is presented, including the PCB design, lumped circuit components, and the overall resonator configuration.

3.1 Loss Tangent

A real capacitor deviates from the ideal behaviour due to energy losses in both the dielectric and the conductive elements. These losses are accounted for by adding an equivalent series resistance (ESR) in series with an ideal capacitor. The impedance of the varactor, therefore, can be defined as:

$$Z = \frac{1}{\mathrm{i}2\pi \mathrm{C_{var}}} + R_{\mathrm{var}} \tag{12}$$

Here i is the imaginary unit, $\mathrm{C_{var}}$ the ideal capacitance and $\mathrm{R_{var}}$ the equivalent series resistance. While ESR provides a convenient circuit-level representation of losses, the loss tangent $\tan(\delta)$ characterises the intrinsic dielectric properties of the material. It is defined as the ratio of the resistive (real) to reactive (imaginary) components of the total current, quantifying the energy dissipated in a dielectric subjected to a non-ideal capacitor [16, 30]:

$$\tan(\delta) = \frac{\mathrm{R_{var}}}{|\mathrm{X_c}|} \Leftrightarrow \tan(\delta) = 2\pi \mathrm{f C_{var} R_{var}} \tag{13}$$

Here $\mathrm{X_c}$ represents the imaginary and R_{var} the real part of the varactor resistance. The $\tan(\delta)$ experimentally obtained for STO ranges from 0.005 - 0.06 [45]

3.2 QPPA Circuit

The QPPA investigated in this work is an LC resonator circuit inspired by previous work [8] and adapted to the present implementation [16]. The device can be operated in both reflection (with red dashed box) and transmission (without it) configurations (Fig. 8). To enable DC biasing of the varactor while preventing direct grounding of the bias line, an additional shunt capacitor C_s is included in the circuit. An inductor L_{RFB} prevents RF signals from propagating into the DC bias line.
The ideal circuit representation, shown in Fig. 8, consists of a parallel LC resonator formed by

an inductance L_1 and a voltage-dependent varactor capacitance C_{var}. In this simplified model, all components are assumed to be lossless, and no parasitic elements are considered, such that the resonance frequency determined solely by the inductance and capacitance.

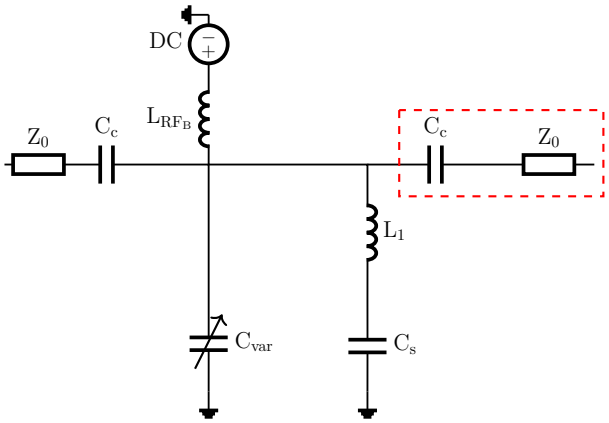

Figure 8: The LC resonator circuit is depicted schematically. The elements enclosed by the red dashed box are included for transmission measurements and absent for reflection measurements. The input load Z_0 is coupled to the resonator, which consists of an inductor L_1 and a varactor C_{var}. The capacitor C_s blocks DC from ground while allowing biasing of the varactor, and the inductor L_{RFB} prevents RF signals from propagating into the DC bias line.

In reality however, non-ideal effects must be taken into account. Both L_1 and the C_{var} exhibit finite series resistances that introduce dissipative losses and contribute to the real part of the circuit impedance. Furthermore, parasitic capacitances C_{par} arising from the device structure, component packaging, and PCB layout modify the resonance characteristics and limit the achievable performance of the QPPA. To obtain a more accurate description of the device, a refined circuit model including the relevant resistive losses and parasitic elements is considered:

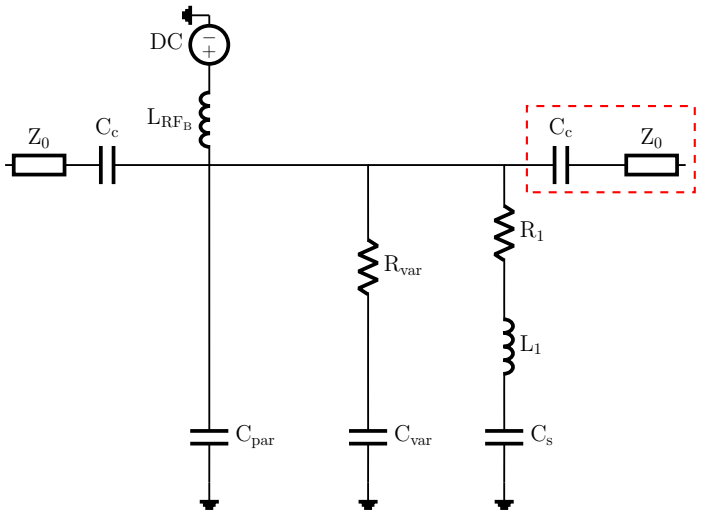

Figure 9: A refined circuit model, which considers series resistance of inductor L_1 (R_1) and varactor C_{var} (R_{var}), and parasitic capacitance (C_{par}) is shown.

The circuit impedance Z of the refined circuit is calculated as:

$$\mathrm{Z_L} = \frac{1}{\mathrm{i2\pi fC_c}} + \left(\frac{1}{\mathrm{i2\pi fL_{RFB}}} + \frac{1}{2\pi \mathrm{fC_{par}}} + \frac{1}{\mathrm{R_{var}} + \frac{1}{\mathrm{i2\pi fC_{var}}}} + \frac{1}{\mathrm{R_1} + \mathrm{i2\pi fL_1} + \frac{1}{\mathrm{i2\pi fC_s}}}\right)^{-1} + \boxed{\frac{1}{i2\pi f C_c}} \tag{14}$$

Knowing Z enables us to calculate the reflection (Γ_R) and the transmission coefficient (Γ_T) with the following equation:

$$\Gamma_R = \frac{Z_L(\omega) - Z_0}{Z_L(\omega) + Z_0} \qquad \Gamma_T = \frac{2Z_L(\omega)}{2Z_L(\omega) + Z_0} \tag{15}$$

and convert them to dB

$$\Gamma_{R_{dB}} = 10 \cdot \log\left(\left|\frac{Z_L(\omega) - Z_0}{Z_L(\omega) + Z_0}\right|\right) \qquad \Gamma_{T_{dB}} = 10 \cdot \log\left(\left|\frac{2Z_L(\omega)}{2Z_L(\omega) + Z_0}\right|\right). \tag{16}$$

$\mathrm{Z_0}$ is the standard 50Ω resistance.
$\mathrm{C_{par}}$ and $\mathrm{R_1}$ was determined in prior work [16] by replacing the varactor with a fixed, known capacitance. After knowing $\mathrm{C_{par}}$ and $\mathrm{R_1}$, we determine $\mathrm{C_{var}}$ and $\mathrm{R_{var}}$ by applying the circuit equation to the $\mathrm{S_{11}}$ and $\mathrm{S_{12}}$, because the capacitor C and R can not be determined with an accuracy higher $\leq 1\,\mathrm{pF}$ before measuring. Example fits can be seen in Fig. 16.

3.3 PCB and circuit

Fig. 10 shows the QPPA circuit board with its lumped components. The STO varactor chip is glued onto the PCB with PMMA. The lumped elements are soldered onto the board using tin to reduce bond interface resistance. The circuit is an LC resonator, comprising an inductor $\mathrm{L_1}$ in parallel to a varactor $\mathrm{C_{var}}$. A DC bias voltage adjusts the varactors' capacitance. The DC path to ground is blocked by a shunt capacitor C_s. An inductor $\mathrm{L_{RFB}}$ prevents RF signals from propagating into the resonator from the DC source. RF tones are injected into the LC resonator via a coupling capacitor ($\mathrm{C_c}$). Together with L_{RFB}, the $\mathrm{C_c}$ capacitors form a bias tee that enables simultaneous application of DC and RF (signal and pump) to the varactor.

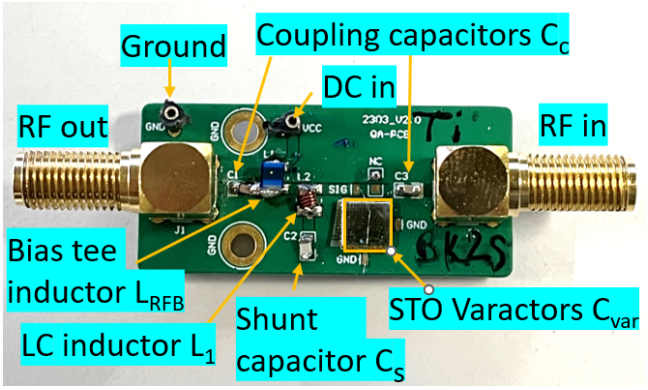

Figure 10: The QPPA PCB is depicted together with its lumped-element components. In the configuration shown, the device is characterized in transmission mode. If one of the two C_c is removed, the device operates in reflection mode.

A schematic representation of the circuit is given in 11. The PCB can operate in reflection mode (without the red dashed box) as well as in transmission mode (with it).

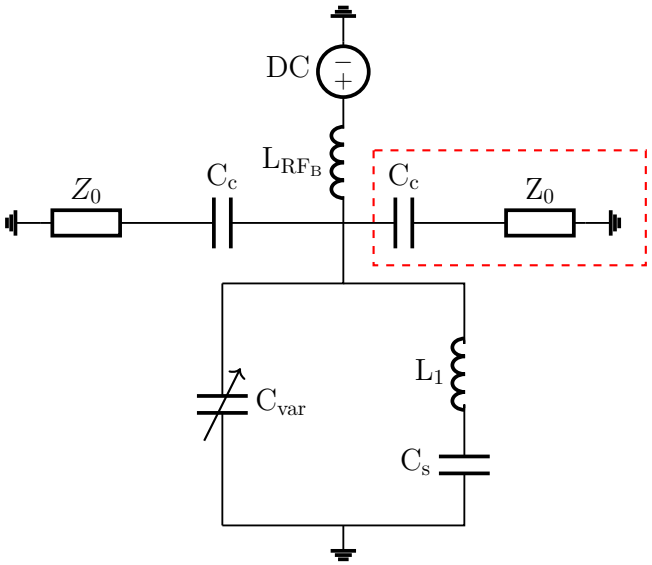

Figure 11: Schematic layout of the QPPA circuit is shown for transmission mode. When removing the components in the red dashed box we are in reflection mode.

The circuit components values used in this project are summarized in the table below:

Capacitor	$C_{par} = 4.085\,pF$	$C_c = 10\,pF$	$C_s = 300\,pF$	C_{var} = from fit
Inductor	$L_1 = 12.1\,nH$			$L_{RFB} = 1000\,nH$
Resistor	$R_L = 0.085\,\Omega$	R_{var} = from fit		

Table 2: The circuit component values are summarized.

3.4 STO Varactor

The varactor structure is composed of STO (dielectric substrate)[4], an optional adhesion layer, and coplanar gold capacitor electrodes sputtered on top of the stack, as schematically depicted in Fig. 12. A comprehensive description of the fabrication process can be found in the Appendix 6.5.

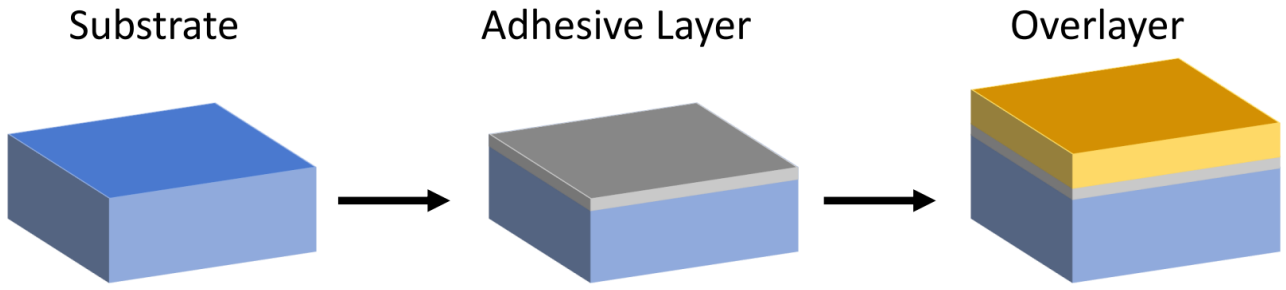

Figure 12: Schematic visualization of the varactor layering process. The substrate is the dielectric STO, the adhesive layer is Ti and the overlayer is Au.

[4]STO [001] was patterned on the polished side.

Figure 13a presents a top-view schematic of the coplanar ring varactor geometry. It consists of two electrode plates. The illustrated geometry uses a circular layout. However, oval ring layouts were also evaluated, since they can be bonded more easily without shorting the varactors. The outer ring has a width of t = 50 μm, while the inner ring has a radius of r = 60 μm. The separation gap between the two electrodes is 0.5μm $\leq$d $\leq$ 5 μm. A cross-sectional view of the device is shown in Fig. 13b. The STO crystal has a thickness of 0.5 mm. On top of the STO, an optional 5 nm adhesion layer is deposited, followed by 65 nm thick gold electrodes.

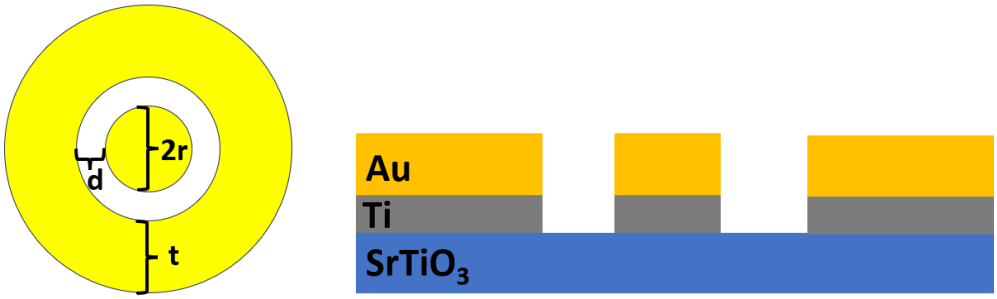

(a) (b)

Figure 13: **a**) Top view of the STO varactor design. The structure consists of a circular outer ring with width **t**, an inner ring with radius **r** and a separation gap **d** between the two electrodes. **b**) A side view of the corresponding varactor.

4 Results and Discussion

All measurements were conducted at liquid helium temperature at approximately 4.2 K using an RF dipstick, if not mentioned otherwise. All QPPAs were designed, as presented in Fig. 13a, apart from one Au/Cr device (see Appendix Fig. 45). The devices were first characterised in reflection mode to get an understanding of what parameters are relevant in characterising parametric amplification (PA) performance for the different materials. Second, transmission measurements were conducted to investigate the PA performance. An exemplary dataset is shown for an Au/Cr device in chapter 4.1,4.2 for a better understanding of the analysis in subchapter 4.3. Third, a systematic comparison of different electrode stack devices was conducted. Fourth, the impact of decreasing inductance L_1 on PA and f_{res} was investigated, with the aim to push for higher frequencies. Fifth, magnetic field dependence measurements were done in a variable temperature insert (VTI) dewar for an Au/Ti device. Sixth, the impact of varying gap sizes was investigated. And finally, some device anomalies are reported.
The regular circuit configuration used for the QPPA is listed in Tab. 2.

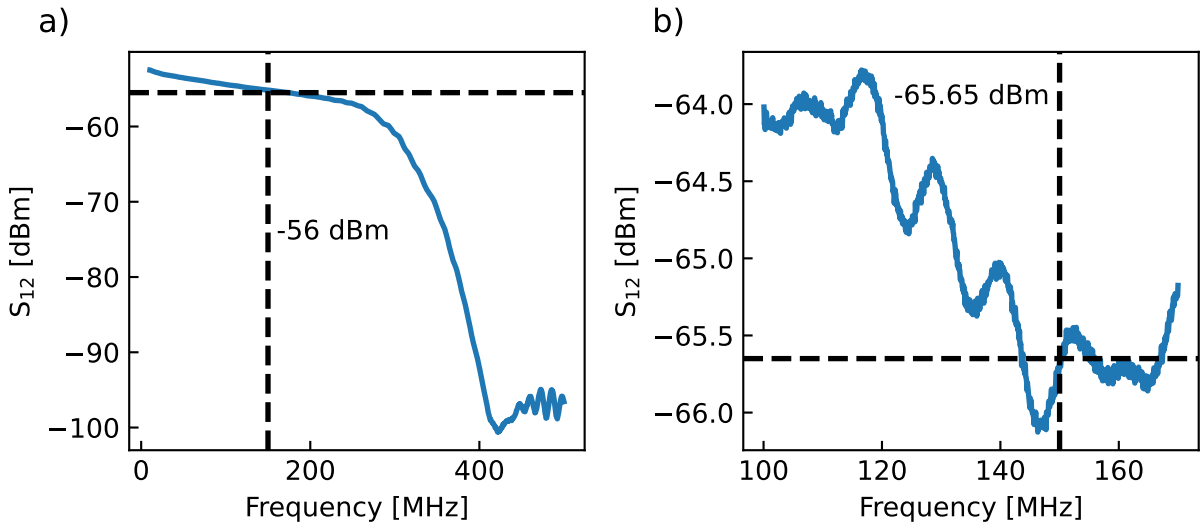

Figure 14: The attenuated source signal amplitude was measured for the shorted line to obtain total setup losses of 12 dBm for signal, and 1 dBm for pump power from the coupler. For RF dipstick in **a)** also 3 dBm signal is lost parasitically and for the VTI in **b)** 8 dBm is lost from the built in attenuator and 5.65 dBm parasitically.

The losses of the measurement lines was determined by shorting the two SMA lines and sending a signal tone with P_{sig} = -40 dBm through. In the measurement setup 16 dBm signal and 1 dBm pump from the coupler is lost. So no signal is lost parasitically in the RF dipstick setup (Fig. 14a), because we send -40 dBm signal in and get -56 dBm signal out. In the VTI (Fig. 14b) 8 dBm attenuation was added, so 1.65 dBm (-65.65 dBm = -40 dBm - 16 dBm - 8 dBm - 1.65 dBm) is lost from the setup parasitically.

4.1 Reflection

In reflection mode the S_{11} parameter is measured using a vector network analyser. DC voltage V_{var} is applied to the varactor with the UHFLI (see Appendix 44).
The chapter presents the relevant reflection measurements performed on the QPPA. These measurements provide insight into the behaviour of the device and establish the experimental basis for the analysis discussed in the following chapters. An exemplary device (Au/Cr 2) was

used to acquire most of the data shown in this chapter [5] .
First, the QPPA resonance frequency f_{res} was measured as a function of DC bias V_{var}. Here, V_{var} was swept from 0 → 5 → -5 → 0 V. This specific V_{var} sweeping pattern was chosen to determine the magnitude of hysteretic effects due to oxygen vacancies, trapped charges and defects [38, 51, 77, 78].
Figure 15 only shows the sweep from 5 → -5 V. From this figure it becomes clear that the DC voltage reaches the varactor, as the resonance frequency f_{res} changes ($f_{res} = 1/2\pi\sqrt{LC_{var}}$). This figure can be understood as a collection of many 1D reflection spectra taken at different bias voltage.

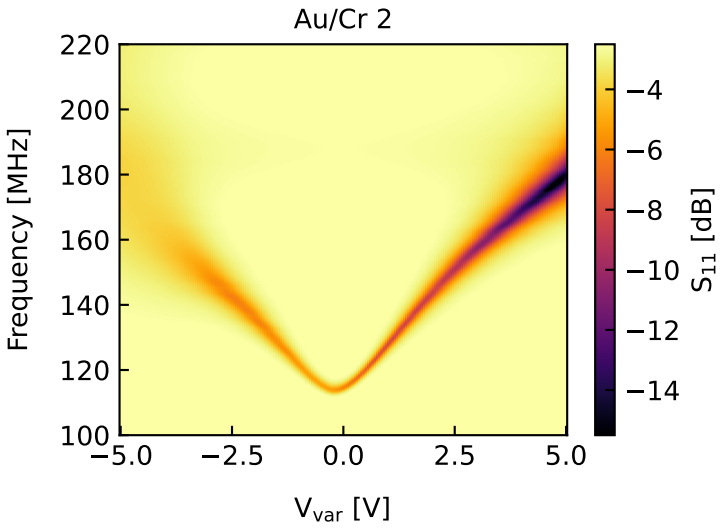

Figure 15: The QPPA reflection spectra as a function of applied DC voltage (V_{var}) is shown. The voltage was swept from 5 → -5 V.

Fig. 16 shows two representative 1D cuts taken from the 0→5 V trace at $V_{var} = 0$ in 16a) and at $V_{var} = 0.5$ in 16b). By fitting the circuit model 14 to the spectra the varactor capacitance C_{var} and resistance R_{var} is determined[6].
From the S_{11} coefficient, it becomes clear that the device is not well impedance matched at 0 V, but as V_{var} increases, the impedance matching improves. Perfect impedance matching was not the primary focus, as long as the signal sufficiently passed through the system. This is because mismatch does not affect the intrinsic parametric amplification mechanism. Hence, this work focused on understanding the impact of different electrode stack compositions on the PA performance. However, impedance matching affects transmission efficiency and the magnitude of the reflected signal.

[5] All measured devices are tabulated in Tab.4)

[6] The parasitic capacitance C_{par} was determined in prior work experimentally by replacing the STO with a known fixed capacitance(C_{par} =4.058 pF).

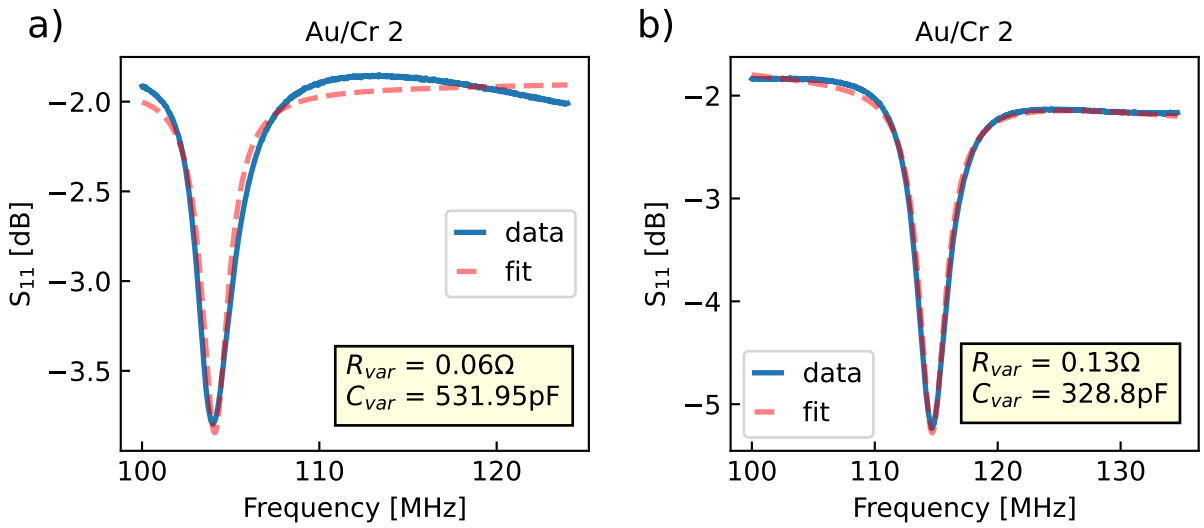

Figure 16: Exemplary reflection spectra from Fig. 15 are shown for 0 V_{var} in **a)** and 0.5 V_{var} in **b)**. By applying the circuit model 14 to the S_{11} data, R_{var} and C_{var} were determined.

The C_{var} obtained from the fit is plotted as function of V_{var} in Fig. 17. At zero bias the maximum capacitance is $C_0 = 531.95$ pF at $f_0 = 104.00$ MHz. Getting back to zero bias after a 5 V exposure the capacitance is reduced to $C_{return} = 328.80$ pF with f_{return}=114.80 MHz. This behaviour is expected for STO, which reduces C_{var} for applied V_{var}. For positive bias exposure up to 5 V, the capacitance tunability reduces to $C_0/C_{return} = 0.61$ due to trapped charges and oxygen vacancies [45, 49, 52, 53]. For negative bias exposure, $C_0/C_{return} = 0.35$. Since C_{var} is the variable component in the LC circuit, it is the driving factor for PA performance. Therefore, from this point onward only the positive bias region is investigated to keep C_{var} tunability, C_0 and the CV slope steepness maximal. In previous work it was determined that operating at the lowest possible bias maximizes C_{return} [17]. Consequently, the range of operation is restricted

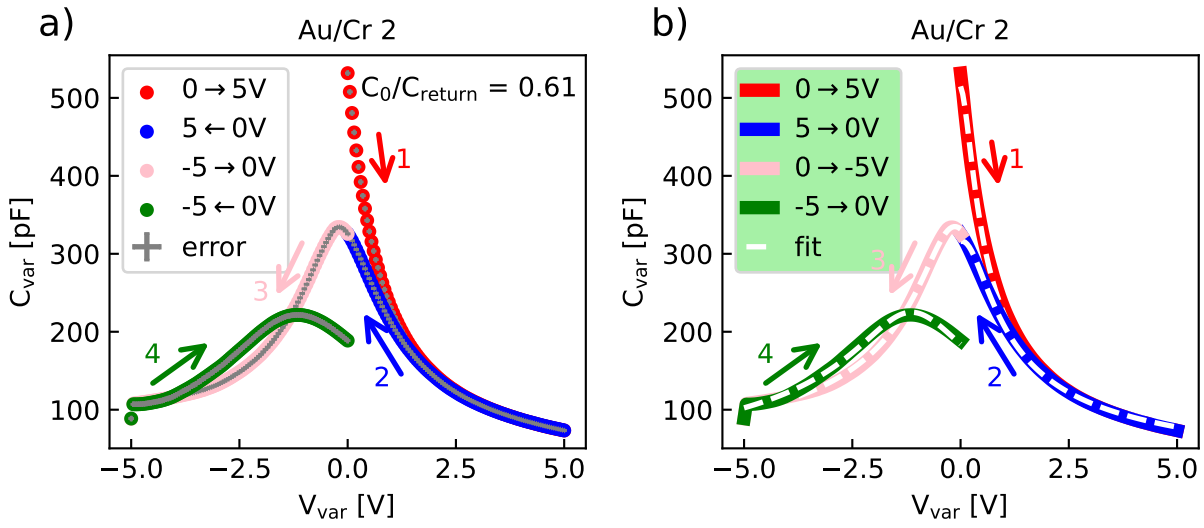

Figure 17: **a)** The varactor capacitance C_{var}, obtained from Fig. 16, is plotted as function of V_{var}. V_{var} was swept from the red to the green trace. The C_{var} tunability reduces to $C_0/C_{return} = 0.61$ upon +5 V exposure. **b)** Equation 11 was fitted to the capacitance curve to describe the C_{var} behaviour theoretically, which suits very well.

to the range 0 to 2 V.

At V_{var} = -5 V a sudden kink in capacitance is observed, which is due to the spectra broadening, reducing the reliability of the analysis[7]. This could be due to lattice distortions and trapped charges for increasing bias [45, 49, 52, 54–57]. As a consequence, the total polarisation becomes less stable. This kink is irrelevant because it is outside the operating bias region for PA. This kink is not typically seen, but does occur sometimes at V_{var} >3 V.
Fig.18a shows the numerical derivative of C_{var} with respect to V_{var}. This figure gives insight into the C_{var} tunability of the device at a given DC bias, i.e. how strongly C_{var} can be modulated for a given bias. It also indicates the bias region in which the QPPA is expected to have the best PA performance, based on where the maxima and minima are. For this device it would be expected to be in the range 0 to 2 V_{var}.

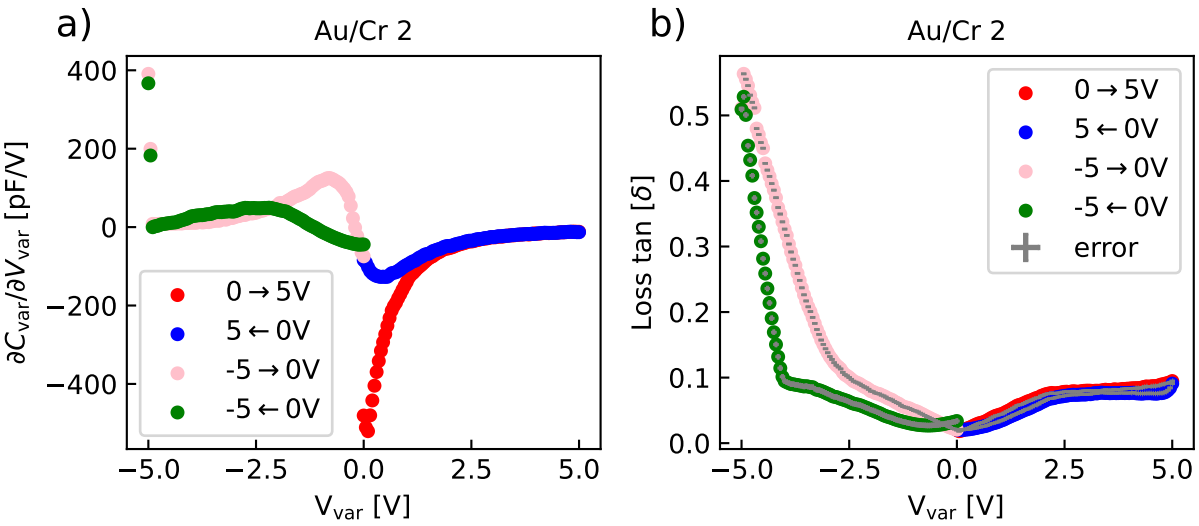

Figure 18: **a)** The derivative of C_{var} from Fig. 17 as function of V_{var} is shown. **b)** The loss tangent derived by computing the R_{var} from the fit (Fig. 16) into equation 13 is shown as function of V_{var} is shown.

Fig. 18b shows the loss tangent tan(δ) as function of V_{var}. The tan(δ) is directly correlated with R_{var} according to equation 13. At zero bias the loss tangent is tan(δ) = 0.02. As V_{var} increases tan(δ) also increases. There is hysteretic behaviour observed for the resistance in the negative, but not the positive bias region, for this particular device. Other Au/Cr devices show tan(δ) values between 0.02 to 0.04 with hysteresis in the order ±0.01 (at zero field).
Values down to 0.005 was already reached experimentally with superconducting electrodes [45]. Here the tan(δ) values are a factor of 3 to 8 higher for zero bias, because the total resistance is taken in this work (e.g. bondwire resistance). An additional reason for increased tan(δ) could be because the Cr sticking layer interfuses with the Au electrodes and creates doping effects or alloy formation [74]. Or it could be some of the chemicals used in the fabrication process, in addition to the Au electrode resistance itself. Chapter 4.3 will compare the impact of sticking layers on the tan(δ).

[7]The fit suits well and the error is much smaller than the value, as can be seen from the error bars.

Key Message

- The STO varactor is tunable and behaves as expected, based on the reflection characterisation.
- STO polarisation depends on the history of the externally applied DC bias.
- Increasing V_{var} increases the $\tan(\delta)$.

4.2 Transmission

In transmission mode the signal tone is generated and recorded by the ultra-high-frequency lock-in amplifier (UHFLI) from Zurich Instruments. The amplitude of the signal for all measurements is set to $P_{sig} = -40\,\text{dBm}$, unless mentioned otherwise. The pump tone is provided by a Rhode & Schwarz SGS100A. Signal and pump tones are combined at room temperature using a Mini-Circuits power splitter (ZN30-17-5-S+). An auxiliary output of the UHFLI is used to apply DC voltage V_{var} to the varactor. The relative phase between signal and pump is controlled via the Zurich Instruments LabOne API(Application Programming Interface)(see setup in Appendix Fig. 43).
This chapter will present what transmission measurements were conducted on a Au/Cr[8] device to characterize its PA performance based on its effective gain G_{eff}. G_{eff} is differentiated into the degenerate G_d and non-degenerate gain G_{nd}. For G_d both the signal tone frequency f_s and the pump frequency f_p are fixed ($2f_s = f_p$) and the clocks of SGS100A and UHFLI synchronized to have a constant relative phase ϕ, which is then swept. For G_{nd}, the f_p is fixed and f_s swept, disregarding ϕ. When talking about gain in this chapter, the losses from the setup and device are accounted for as mentioned in chapter 4.

4.2.1 Parametric Amplification

Fig. 19 is the most informative plot, revealing whether a device can provide parametric amplification of a signal tone. If so, it maps out the optimal operating condition in terms of both the voltage range and the corresponding signal frequency at which the gain is maximised. In this figure, the gain is plotted as a function of V_{var} over the range from 0 to 2 V.[9]. In this measurement, the pump frequency f_p is set to twice the signal frequency f_s and both frequencies are simultaneously swept, while the pump power is kept constant at $P_p = 25\,\text{dBm}$. This spectrum looks noisy, because the relative phase between pump and signal tone is not fixed, meaning destructive and constructive interference occur uncontrolled. The white dots indicate where further high-resolution measurements were conducted. The plots presented in chap. 4.2.2 were taken at $V_{var} = 1.4\,\text{V}$ (indicated by the blue circle in Fig. 19).

[8]Same device as in reflection, but with an additional coupling capacitor.

[9]Complete measurement covered 100-200 MHz and 0-3 V, however, only the range showing significant gain is presented.

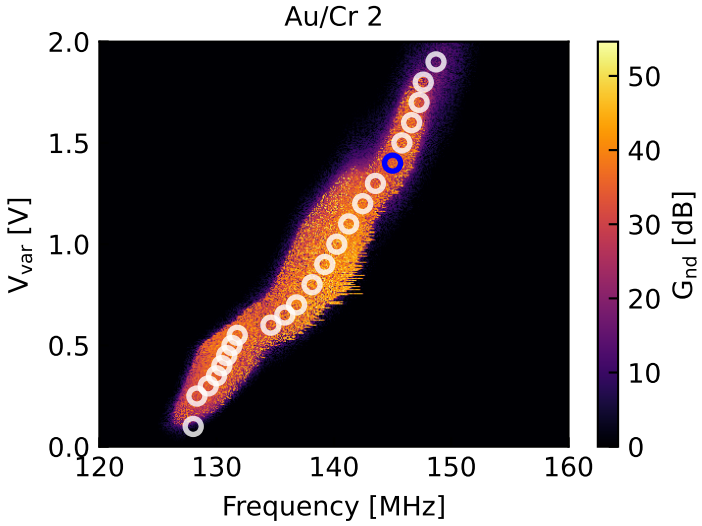

Figure 19: The gain as a function of voltage is shown. Here the pump power was set to $P_p = 25\,dBm$. The f_s was fixed to half of f_p and both frequencies were simultaneously swept. The white circles indicate areas were high resolution measurements were conducted. The blue circle represents the area of the high-resolution measurements, which are presented chap. 4.2.2.

4.2.2 Non-Degenerate Gain

The plots presented below were taken at $V_{var} = 1.4\,V$ (indicated by the blue circle in Fig. 19). Fig. 20a shows the non-degenerate gain near the resonance frequency as a function of P_p. The gain increases up to an optimal P_p, reaching a maximum of $G_{nd} = (31 \pm 1)\,dB$ at $f_s = 145\,MHz$. Above $P_p = 22.4\,dBm$ G_{nd} decreases rapidly again. This behaviour is due to the capacitance modulation oscillating in the positive and negative bias region along the CV curve. This is explained in chap. 2.5.

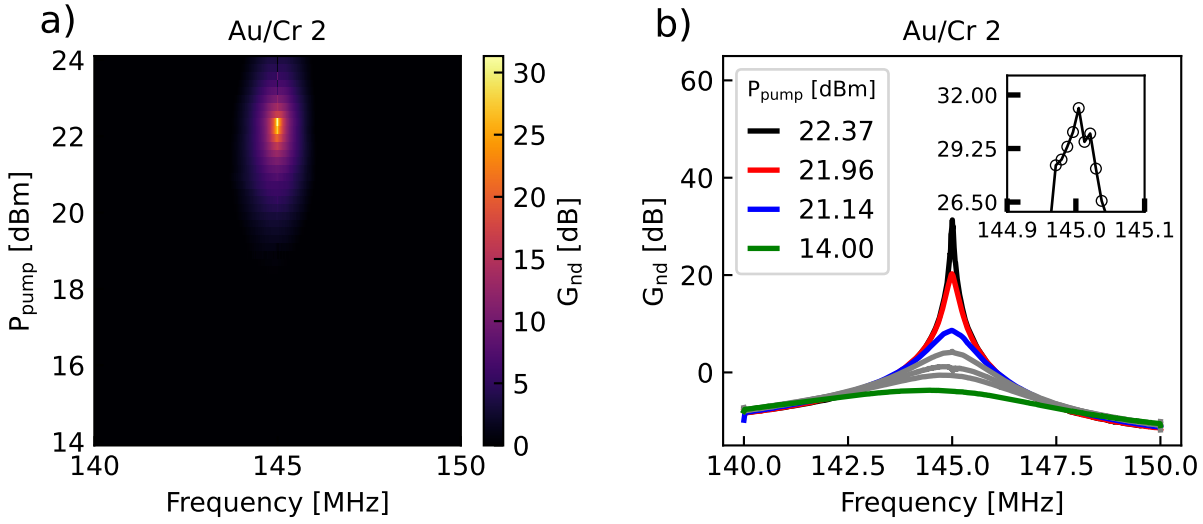

Figure 20: **a)** The gain as a function of P_p is shown. **b)** The 1D traces extracted from **a)** are presented for increasing P_p. On the top left a zoom-in of the maximum peak (black trace) is shown, to indicate a non-Lorentzian shape.

Fig. 20b shows 1D gain traces taken from Fig. 20a to showcase how increasing P_p enhances the signal tone amplitude. At first glance, the maximum peak appears to be typical Lorentzian, but upon closer inspection, it becomes evident that the peak shape is unusual (zoom-in in Fig. 20b). These unconventional peak shapes can only be observed when the frequency step size is chosen small enough and P_p high enough to achieve $G_{nd} \geq 25\,dB$. The peak shape and and its evolution will be further discussed in chapter 4.3.1.
Fig. 21 shows the extracted maximum values from Fig. 20a as function of P_p. A minimum threshold pump power of $P_{threshold} = 18.5\,dBm$ is needed to start generating effective gain, $P_{10dBm} = 21.3\,dBm$ for 10 dB and $P_{20dBm} = 22\,dBm$ for 20 dB gain. The P_{20dBm} values will be investigated more carefully to benchmark different devices in chapter 4.3.

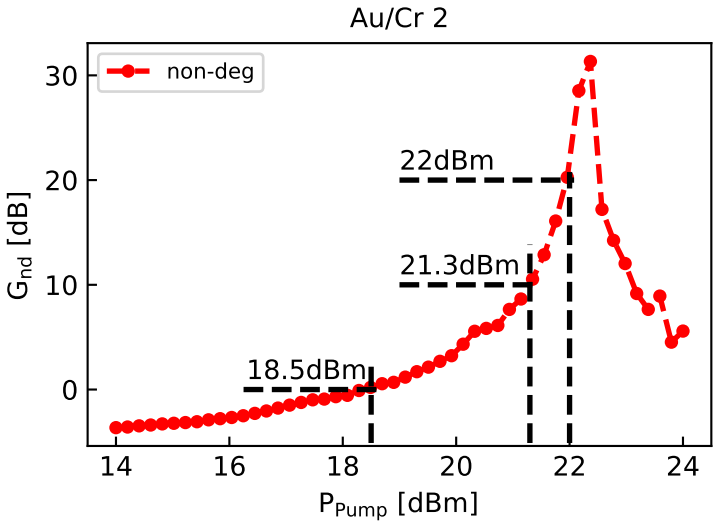

Figure 21: The maximum amplitude is extracted from Fig. 20a and plotted as a function of P_p. At P_p=18 dBm the QPPA starts generating effective gain, at P_p=22.3 10 dB and at P_p=23 dBm 20 dBm gain.

4.2.3 Degenerate Gain

In this chapter, the influence of the relative phase ϕ between the signal and the pump tone on the gain is examined. Figure 22a shows the degenerate gain as a function of ϕ for increasing values of P_p. For P_p up to $G_d \approx 20\,dBm$, the behaviour can still be well described by three-wave mixing, because the cosine fits well to the pink trace (see Fig. 22c). In this regime, the underlying physics is well understood. Once $G_d > 20\,dBm$ is reached, however, the response deviates from a purely cosine-like dependence and exhibits an unfamiliar phase sensitivity. In this high-gain regime, at a particular ϕ, the gain is maximised. Moving away from this ϕ reduces the gain, but does not fully suppress it. The current interpretation is that, at sufficiently high P_p, higher-order non-linear terms of the STO start to contribute and interfere with the usual signal-pump mixing mechanism. Furthermore, for achieving gain around $G_d \geq 40\,dBm$ the amplitude becomes noisy. This may be because energy transfer from pump to the STO is inefficient and/or insufficient to sustain such a high gain, except at a single mode (the peak). Or because the STO reached its maximum 3-wave-mixing potential[10], leading to dissipation

[10]For the given design and conditions (e.g. impedance mismatch, electrode stack impurities etc.) of the QPPA.

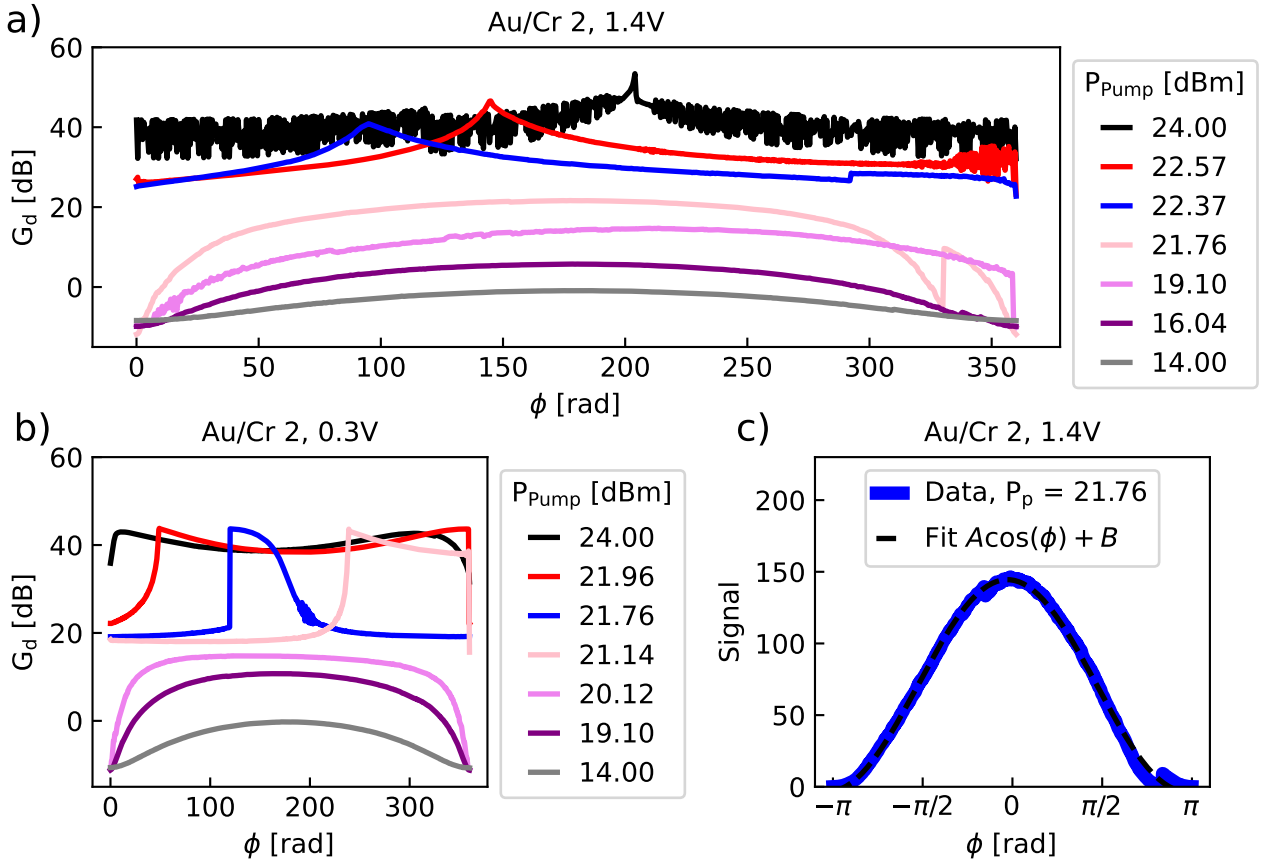

Figure 22: The degenerate gain as function of relative phase is shown for $V_{var} = 1.4V$ in **a)** and $V_{var} = 0.3V$ in **b)** to showcase different shapes.**c)** A cosine fit was applied to the violet trace from Fig. **a)** to showcase the 3-wave mixing mechanism.

of excess P_p. As a consequence, the physical conditions change because energy is dissipated through electrostriction or the inverse piezoelectric effect, as well as through RF signal-phonon interactions, leading to distortion or intermodulation [30, 59]. Consequently the signal becomes unstable.

Fig. 22b shows the phase traces recorded at $V_{var} = 0.3\,V$, illustrating the variety of phase shapes measured. In the blue trace, for less P_p, there is a slightly noisy area, indicating that the previously made presumptions are not fully correct and some, at this moment unidentified, conditions have to be met for the noisy traces to appear.

4.2.4 Degenerate vs Non-Degenerate Gain

In Fig. 23, the difference between the degenerate and non-degenerate gains as a function of increasing P_p is shown. The peak values extracted from Fig. 22a represent the G_d (blue trace). The G_d is always higher than G_{nd}. The convergence of the G_d at higher P_p indicates that the potential limit for the current varactor and circuit design and measuring conditions is reached. The surprising thing about this figure is that the maximum G_{nd} is already reached at $G_{nd} = 31.33\,dBm$. This is surprising because in Fig. 22a, at a $P_p = 24\,dBm$ a $G_d \approx 40$ to $46\,dBm$ is reached, independent of ϕ. This statement is further supported by Fig. 19, where ϕ was not controlled. This means independent of ϕ the G_{nd} should reach similar values for the high-resolution data presented. This could mean, that when fixing f_p and sweeping f_s the optimum f_{res} is missed, compared to sweeping both frequencies simultaneously (both scenarios for the

condition $2f_s = f_p$).

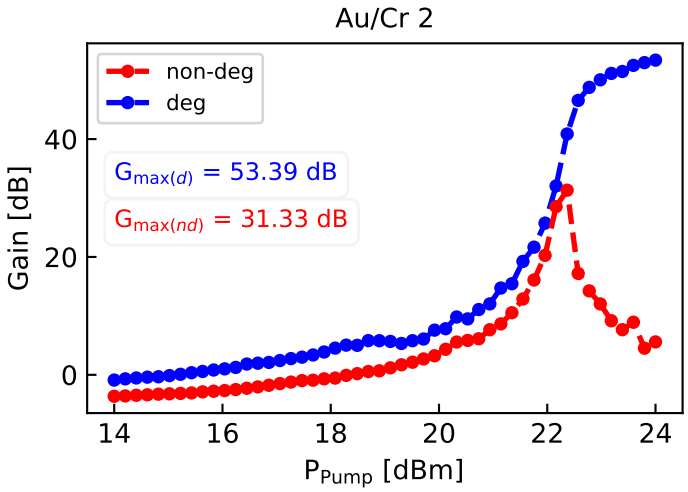

Figure 23: The degenerate vs the non-degenerate gain as a function of P_p is shown. $G_{max(d/nd)}$ stands for the maximum degenerate (d) and non-degenerate (nd) gain measured.

4.2.5 Q-Factor

In order to determine the Q-factor of the QPPA device, the data from Fig. 20b is converted from dB to linear and the following Lorentzian fitted [8]:

$$G(f_{sig}) = G_{offset} + A \cdot \frac{\gamma}{\pi((f_{sig} - f_0)^2 + \gamma^2)} \tag{17}$$

Here, G represents the gain, G_{offset} a global offset, A the peak amplitude, 2γ the bandwidth (BW) at FWHM, f_0 the resonance frequency and f_{sig} the signal frequency. In Fig. 24 the BW is then plotted as a function of the inverse square root of gain. A Q-factor of Q = 14.33 is obtained by applying a linear fit with the below equation, :

$$Q_{res} = \frac{f_{res}}{2BW(G)} \frac{1}{\sqrt{G}}. \tag{18}$$

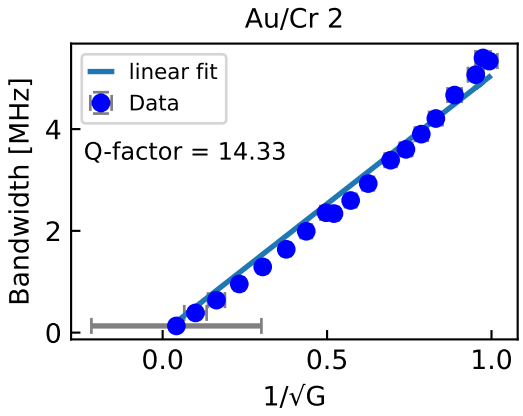

Figure 24: The bandwidth is plotted as a function of the inverse square root of gain. Both values were obtained by fitting equation 17 to the data in Fig. 20b. A linear fit (Eq. 18) is applied to obtain a Q-factor of Q = 14.33.

4.2.6 1dB Compression Point

This chapter investigates the 1 dB compression point for the devices. Figure 25a shows the maximum degenerate gain at $V_{var} = 0.2$ V, extracted from Fig. 46(Appendix), as a function of the signal power[11]. Several gain traces corresponding to different P_p are displayed.
For $P_p \leq 20$ dBm, the gain remains approximately constant at low signal powers P_{sig}. However, when P_{sig} approaches -28.5 dBm, a distinct kink appears and the gain begins to decrease. In contrast, for $P_p = 24$ dBm the trace is almost straight and the kink is barely visible. For intermediate pump powers (21 - 23 dBm), the gain traces gradually converge toward the $P_p = 24$ dBm trace.
Notably, all gain traces collapse onto a single line for $P_{sig} \geq -28.5$ dBm. This indicates that the gain is no longer determined by the P_p but instead becomes limited by the signal power. This is not due to the saturation of the UHFLI input stage, as the saturation power does not increase linearly with the increasing P_p (Appendix Fig. 47). In this regime, the signal may be sufficiently strong to significantly deplete the pump, thereby limiting the achievable gain. Nonetheless, the device reaches a universal gain limit.
At low ($P_{sig} \leq 35$) dBm, the measured gain exhibits an oscillatory and noisy behaviour. This is not due to intrinsic device nonlinearity, but the finite voltage step size limiting the resolution of the applied sinusoidal modulation. In addition, the input signal may be below the noise floor, which further contributes to the observed fluctuations.

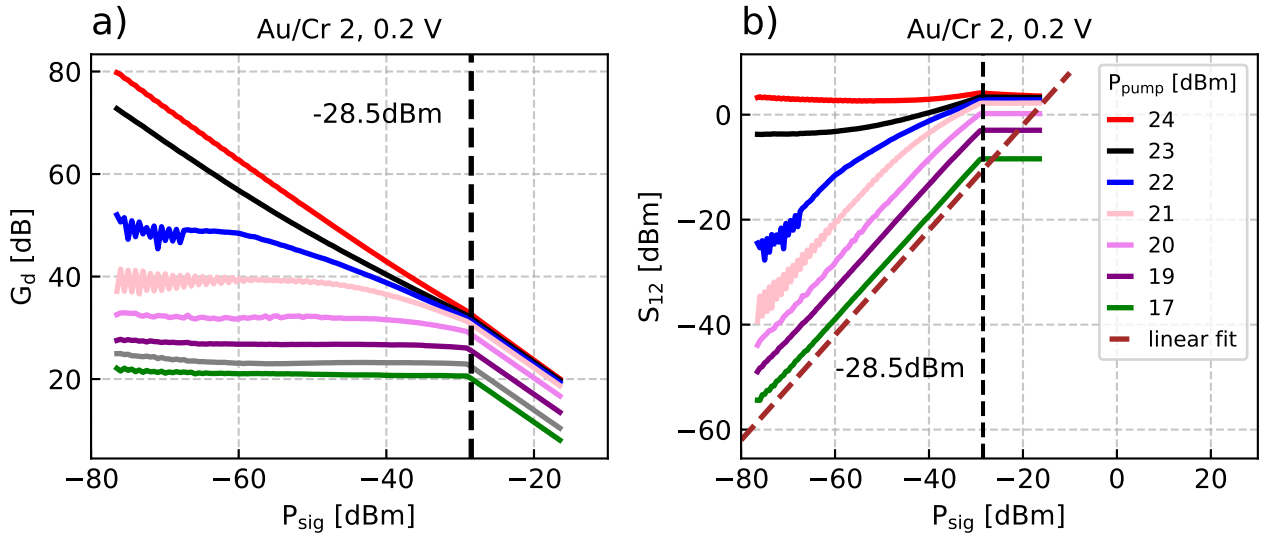

Figure 25: **a)** The gain for various P_p as a function of the input signal power P_{sig} is shown for the device Au/Cr 2 at $V_{var} = 0.2$ V. **b)** The output signal power P_{out} (S_{12}) for various P_p as a function of the input signal power P_{sig} is shown for the device Au/Cr 2 at $V_{var} = 0.2$ V. The legend is valid for **a)** also.

Fig. 25b shows the signal output power (S_{12}) as a function of signal input power P_{sig} for different P_p. At low P_p, the S_{12} increases approximately linearly with the input signal power. This is confirmed by the linear fit of slope = 1. At P_{sig} = -28.5 dBm, the amplification abruptly saturates and the output power approaches a constant value, becoming independent of further increases in P_{sig}. Such an abrupt kink is not typically observed in amplifier characteristics. Instead, with increasing P_{sig} the output usually deviates gradually from the initial linear dependence as gain compression sets in, leading to a smooth transition into the saturation regime (see chap. 2.4 or Fig. 27).

[11] See Appendix for a more detailed explanation of how this plot was generated

For higher P_p, the curves start at a larger S_{12} and operate in a strongly non-linear regime (slope ≥ 1). Despite the different P_p, all traces reach saturation at approximately the same P_{sig}. This again shows the onset of gain saturation being determined by the P_{sig} rather than by the P_p. The plot also indicates that the maximum achievable gain may be almost reached at P_p = 24 dBm, as the trace is very close to the saturated gain even for low P_{sig}.

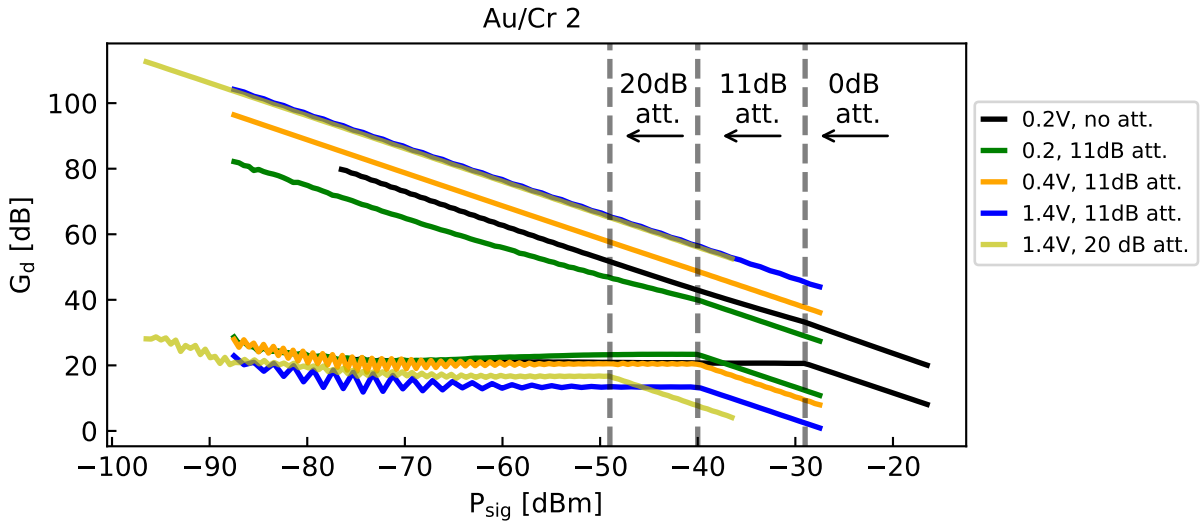

Figure 26: The gain as a function of the input signal power P_{sig} is shown for different V_{var} and attenuation levels. Each colour shows the maximum (24 dBm) and minimum (14-18 dBm) P_p trace.

Figure 26 is the analogue to Fig. 25a, but shows the maximum (P_p = 24 dBm) and minimum (P_p = 14-18 dBm) gain traces measured for different P_p at various DC bias voltages and signal attenuation levels. The aim is to determine whether these parameters influence the position of the kink observed in the gain traces.
The results show that neither the DC bias voltage nor P_p affects the kink position. Instead, the kink shifts only with the applied signal attenuation. Specifically, the kink position moves proportionally with the applied attenuation of P_{sig}, as indicated by the black dashed lines and arrows in the figure. This observation supports the previous statement, that P_{sig} is the only known parameter influencing the kink position. However, the kink is unlikely due to pump depletion. If this were the case, the kink would be expected to appear at the same P_{sig} independent of the applied signal attenuation. Although the overall gain is also affected by attenuation, variation in V_{var} leads to different impedance matching conditions, which complicates a direct comparison. Apart from this proportional shift, no further clear trends can be identified at this stage. Consequently, the underlying mechanism responsible for this behaviour remains unclear and further investigation is needed.

Fig. 27a shows the analogue measurement of Fig. 25, but for the AU/Cr 1 device at V_{var} = 0.48 V. In contrast to the previous case, here the gain first approaches a saturation value. As P_{sig} increases, no abrupt kink is observed. Instead, a gradual transition from linear to the compression region occurs, consistent with the theory [30, 32, 33]. Fig. 27b is an exemplary plot to indicate the 1 dB compression point at -43.95 dBm for P_p = 19.65 dBm. For all the high PA performance devices from this work, these measurements are presented in the appendix Fig. 46. No clear trend or systematic pattern is observed among these devices. However, their

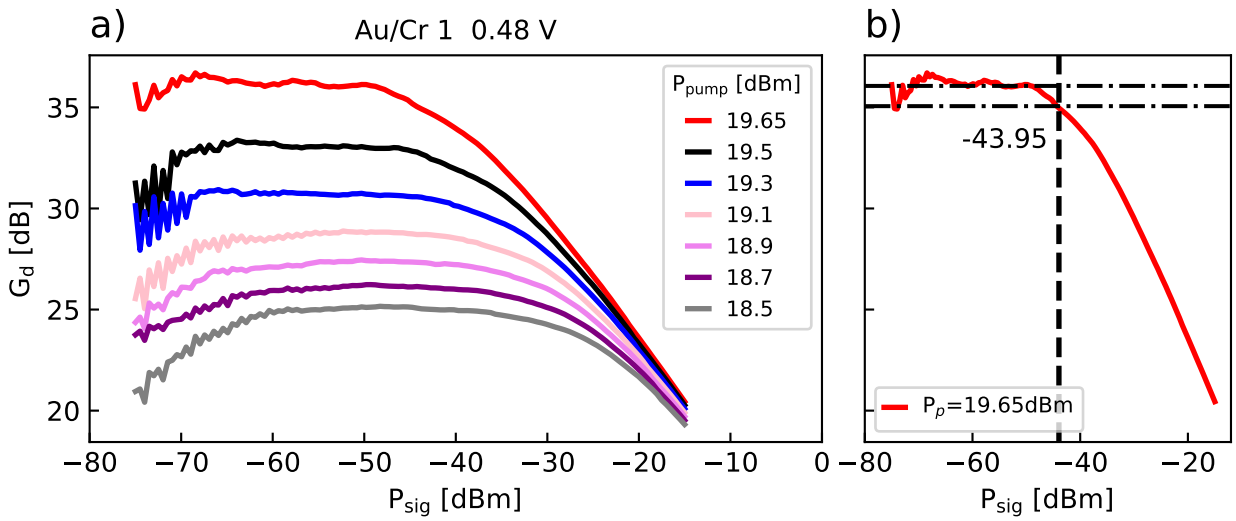

Figure 27: **a)** The gain as a function of the signal input power P_{sig} is shown for various P_p. **b)**The gain trace for P_p = 19.65 dBm is shown. The 1 dB compression point is at -43.95 dBm.

behaviour appears to be strongly dependent on V_{var} , which defines where on the CV curve it is operated at, and the same considerations discussed above for the Au/Cr 2 device apply here as well.

Key Message

- The QPPA achieves gain up to ≈ 54 dBm.
- In the high-gain regime the phase sensitivity is significantly reduced.
- The 1 dB compression point varies inbetween devices in the range P_{sig} = -45 dBm to -30 dBm.

4.3 Material Comparison - Transmission

In the previous sections, the operation of an Au/Cr device was examined in greater detail. This section now focuses on a systematic comparison of the PA performance of devices built with Au and Au/Ti electrode stacks. The goal is to determine how the choice of electrode material and sticking layer affects the device's intrinsic properties and its ability to amplify signals.
The comparison is based only on experimentally measured results. Big emphasis is placed on identifying material-dependent trends in gain efficiency, stability, and reproducibility. Additionally, trends correlating with changes in varactor geometry and operating bias conditions were investigated. By systematically analysing multiple devices (see Tab. 3) per electrode configuration, effects from device-to-device variations were identified.
The data on Au devices have to be taken with caution, as only 2 out of 5 devices achieved noticeable PA and on top of that the working range was very limited to 0.9 - 1.1 V. Furthermore, the data could not be reproduced.

electrode stack	# of devices investigated	gain $\geq 25\,\mathrm{dBm}$
Au	2	0
Au (EBL)	3	1
Au/Ti	3	3
Au/Cr	4	4

Table 3: The types of devices fabricated and the number of measured devices are given. EBL stands for electron-beam lithography. If not labelled they were produced via photolithography.

4.3.1 Non-degenerate Gain

In Fig. 20b, the non-degenerate gain of the Au/Cr 2 device was presented. Now the Au 3 (EBL)(Fig. 28a) and Au/Ti 1 (Fig. 28b) devices are compared to it. For Au a double peak and for Au/Ti a Lorentzian, which is slightly curved to the left, is observed. The slight curving is due to the Duffing non-linearity [23]. When comparing all measured devices one can say that depending on the DC bias all Au/Cr devices, two out of three Au/Ti devices and the single working Au device (Au 3 EBL) showed double peaks (Tab. 4). It is not certain if this behaviour is influenced by the electrode stack configuration or the device-to-device variability. Part of the explanations for the unconventional peaks are signal/phase distortions due to RF-phonon interaction and intermodulation, apart from the higher-order nonlinearity [30, 32, 33]. A little more insight into the resonance peak shapes and evolution is provided in chap. 4.3.2.

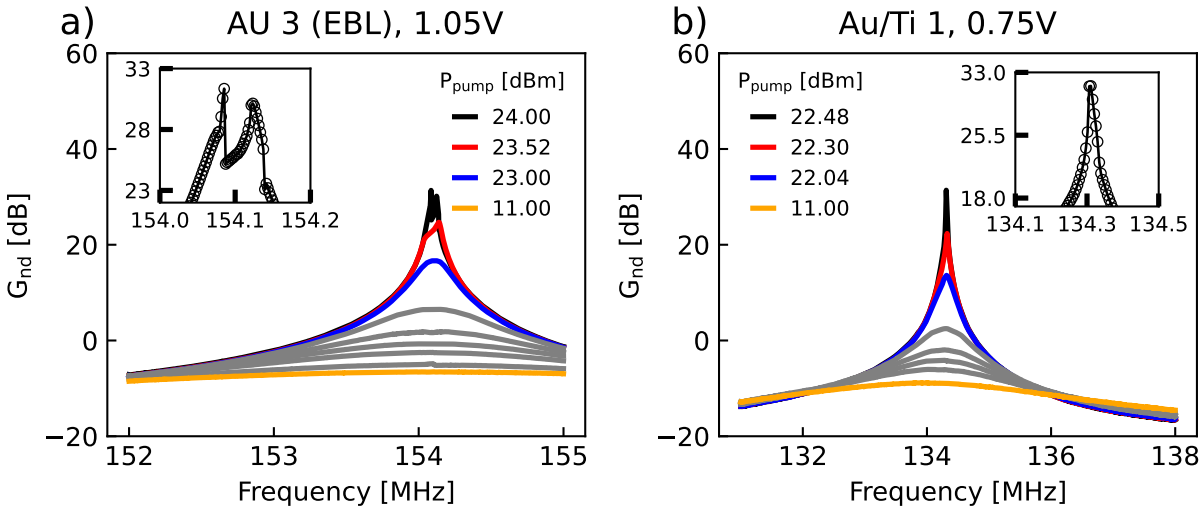

Figure 28: The transmission gain spectra as a function of P_p is shown for Au 3 (EBL) in **a)** and Au/Ti 1 in **b)**. On the top left a zoom-in of the maximum peak (black trace) is shown, to indicate a non-Lorentzian shape.

4.3.2 Resonance Peak Evolution

This chapter provides an overview of how the resonance peak shapes behave and which factors may influence it. Figures 29, 30, and 31 show 1D gain traces recorded at a constant DC bias and fixed f_p, for progressively increasing P_p. For the analysis of the peak-shape evolution, only the traces entering and staying in the high-gain regime are taken into account.
Fig. 29 presents data from the Au/Cr 2 device at different DC bias. In Fig. 29 a-d), the DC bias was fixed to $V_{var} = 0.35\,\mathrm{V}$. Upon entering the high-gain regime, two peaks are visible. Initially, the right peak is dominant and more clearly visible. As the P_p is increased (see

Fig. 29 b-d), the left peak starts to form and overtakes the right peak in amplitude for high enough P_P. What can be said is that for increasing P_p, both peak amplitudes increase, and become more visible. Additionally, the two modes come closer together. The theoretical model in [14] explains this by the appearance of isola and double peaks for large enough P_p (chap. 2.3).

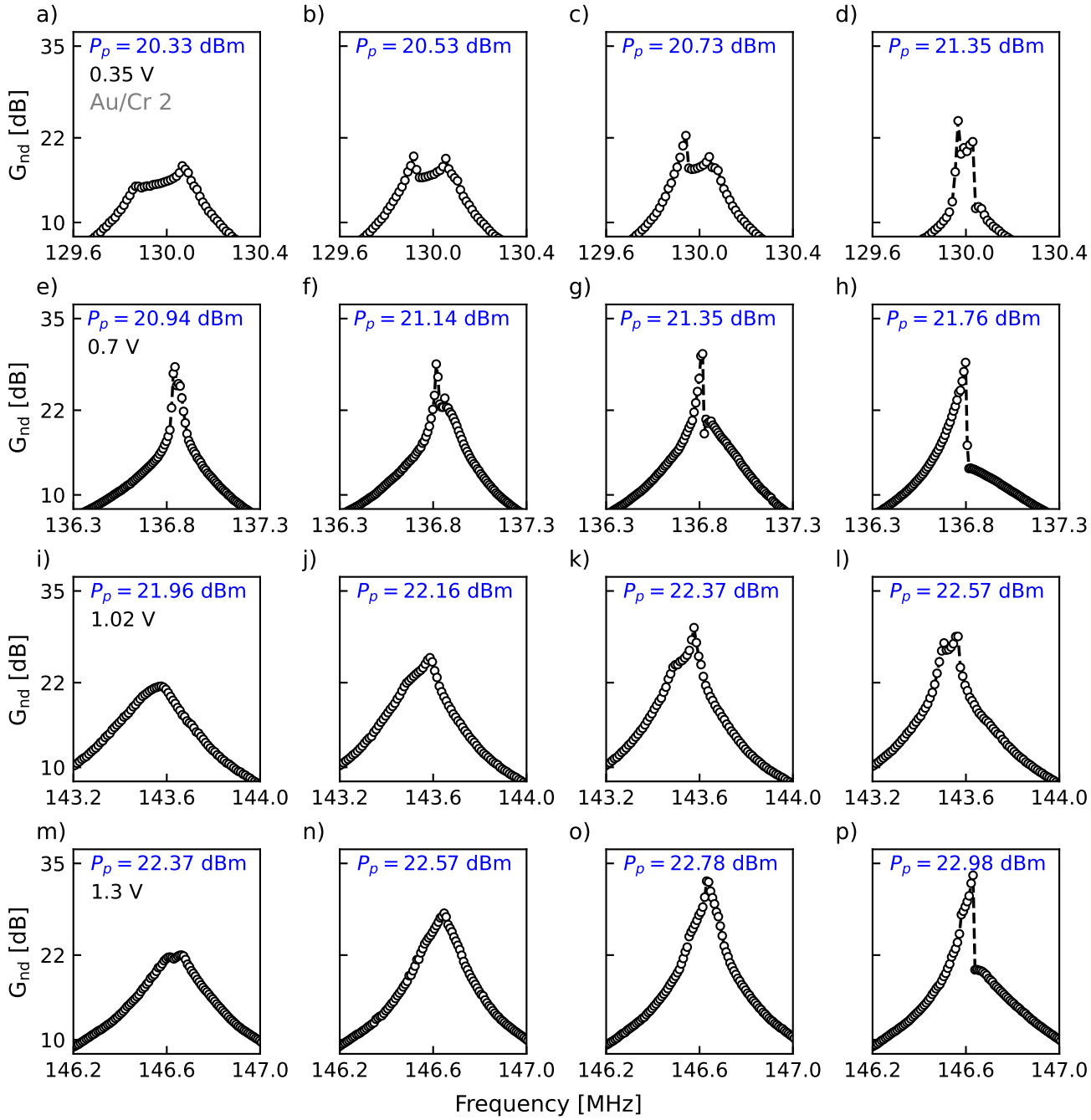

Figure 29: For the Au/Cr 2 device, the gain spectra are shown for a given DC bias (black) with a specific P_p (blue). The plot showcases the evolution of the peak shape as a function of increasing P_p and $V_{var} = 0.35\,V$ in **a-d)**, $V_{var} = 0.7\,V$ in **e-h)**, $1.02\,V$ in **i-l)** and $V_{var} = 1.3\,V$ in **m-p)**.

In Fig.29, panels e-h, i-l, and m-p correspond to DC biases of $V_{var} = 0.7\,V$, $1.02\,V$, and $1.3\,V$ respectively. The DC bias, same as high P_p, influences the resonance frequency, hence may also affects the peak shape. Increasing V_{var} seems to bring the two modes closer together.

However, this trend is not consistent. While some panels follow the expected behaviour, others deviate. For example, panel d already shows two modes, which, for increasing V_{var}, come very close in frequency in panel h. In panel p, the modes approach each other further and begin to merge, accompanied by an increase in gain for both modes, compared to panel h. In contrast, panel l exhibits two clearly distinguishable modes again, indicating a partial separation. The observation suggests that DC bias not only tunes the resonance but maybe also the mode spacing. If the system is over-pumped, the total gain drops sharply, marking the exit from the high-gain regime (not shown here)[12].

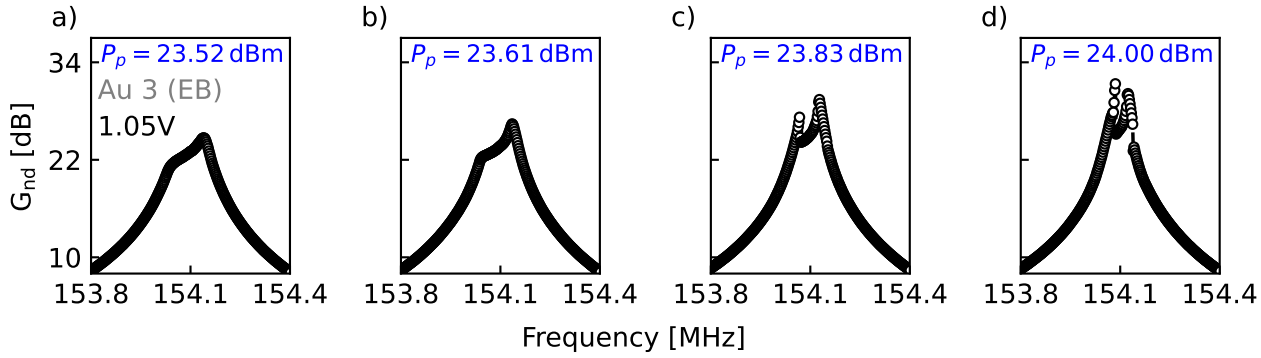

Figure 30: For the Au 3 (EBL) device the gain spectra is shown for $V_{var} = 1.05\,V$ with increasing P_p indicated in blue.

Fig. 30 analogously shows the peak evolution for the Au 3 (EBL) device with no sticking layer at $V_{var} = 1.05\,V$. Compared to Au/Cr 2, it shows the same behaviour as a function of P_p, but the two modes are still distinguishable for $G_{nd} > 30\,dBm$. Here again isola emerge[14]. Regarding the DC bias relation, not much can be said, as this device entered the high-gain regime only at $1.05\,V$ bias[13].

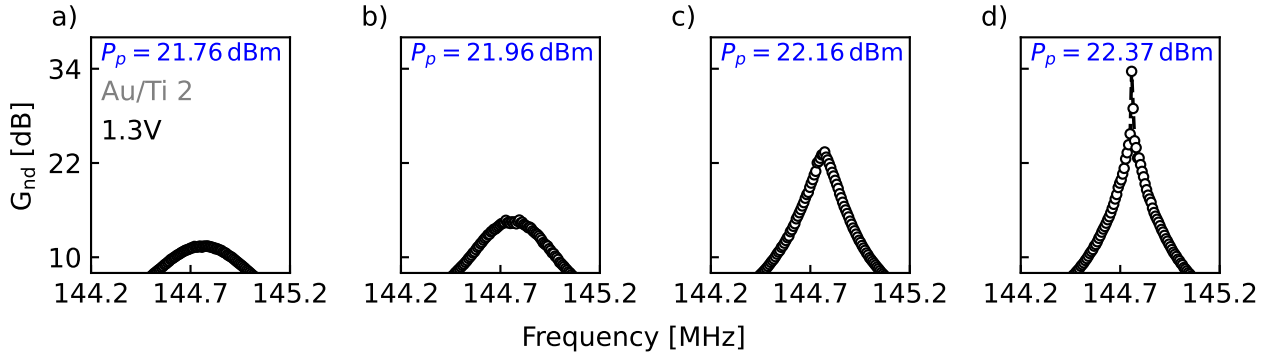

Figure 31: For Au/Ti 2 the gain spectra is shown for $V_{var} = 1.3\,V$ with increasing P_p indicated in blue.

Fig. 31 presents the Au/Ti 2 device at $V_{var} = 1.3\,V$. Here, there is either a single existing mode or the two modes are so close to each other that they can not be distinguished (overlap). Maybe, the maximum gain is reached with less pumping, because the potentially maximum amplitude is lower. This is the reason for this mode looking most Lorentzian. What can be added here is that for two out of three Au/Ti devices, only a single mode was observed. For

[12]The last high-gain trace before exiting is shown in these panels.

[13]Out of 5 Au devices, only the one presented here gave reasonable gain over 25 dBm.

the other one, shapes as for Au/Cr and Au was observed (double peaks), although they were all fabricated in the same batch of STO. It is not known where this inconsistency is originating from. A guess would be that the devices have different material defect density in the QPPA, mainly oxygen vacancies.

Key Message

- Independent of the electrode stack, similar gain can be achieved, but the required P_p varies ($P_{Au/Cr} < P_{Au/Ti} << P_{Au}$)
- The PA response deviates from a Lorentzian behaviour at higher pump powers due to Duffing non-linearity and non-linear damping, creating an isola and double peak in the QPPA response.

4.3.3 Degenerate Gain

In Fig.22a, the degenerate gain of the Au/Cr 2 device is shown. The analogue measurement for the Au 3 (EBL) device at a DC bias of 0.95 V is presented in Fig. 32a.
In this case, the intermediate-gain regime (10 to 20 dBm) is reached with $P_p \geq 21$ dBm[14]. There, the phase sensitivity is present, but the high-gain regime (G $\geq$25 dBm) can not be reached. The traces remained well defined regardless of V_{var}. However, since only two out of five Au devices showed significant G_{nd}, the available data are insufficient for a reliable conclusion. In addition, the functioning Au devices operated only within a narrow voltage window (0.9–1.1 V), in which PA was achieved. Remeasurement of the originally recorded data did not reproduce the initial results, but $G_{nd} < 5$ dBm. The reason for this inconsistency is unclear and requires further investigation.

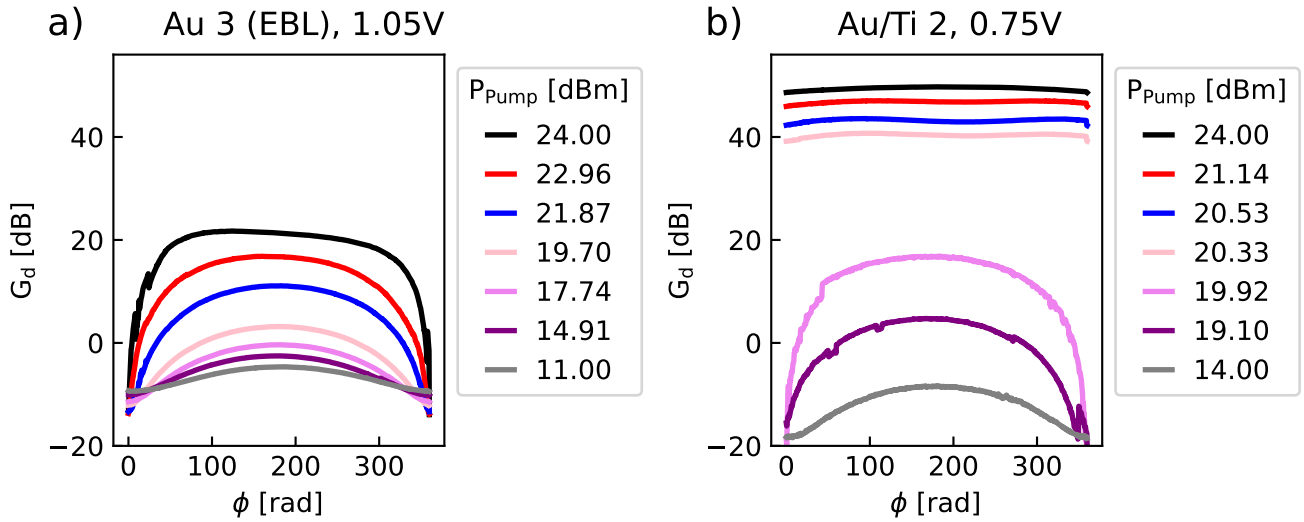

Figure 32: **a)** The gain as a function of the relative phase between signal and pump tone is shown for Au 3 (EBL) at 1.05 V in **a)** and Au/Ti 2 at 0.75 V in **b).**

[14]For all devices measured a pump power of around $P_p \geq 19$ dBm is needed to achieve gain higher 30 dB.

Figure 32b shows the corresponding measurement for the Au/Ti 2 device at $V_{var} = 0.75\,V$, analogous to Fig. 22a. In contrast to the Au device, no pronounced phase sensitivity is observed in the high-gain regime.
Overall, the results suggest that the introduction of adhesion layers in the electrode stack modifies or reduces the phase sensitivity. Both Au/Cr and Au/Ti devices exhibit partially noisy phase spectra at certain V_{var} (see Fig. 22a)[15]. For the Au devices, no noisy phase traces were observed. However, due to the limited dataset, their occurrence cannot be ruled out. A look at Tab. 4 indicates a correlation between the absence of double peaks and the absence of noisy phase spectra once the high-gain regime is reached. An exception is the Au 3 (EBL) devices, exhibiting double peaks in the high-gain regime, with non-noisy phase behaviour. Due to the limited data available for Au 3 (EBL), this device is treated as an outlier and is not considered further in this context.

electrode stack	gap size [μm]	gain$\geq$25 dBm	double peak	noisy phase
Au 1	1	no	-	-
Au 2	1	no	-	-
Au 1 (EBL)	1	no	-	-
Au 2 (EBL)	2	no	-	-
Au 3 (EBL)	0.5	yes	yes	no
Au/Ti 1	1	yes	yes	yes
Au/Ti 2	1	yes	no	no
Au/Ti 3	5	yes	no	no
Au/Cr 1	3	yes	yes	yes
Au/Cr 2	3	yes	yes	yes
Au/Cr 3	-	yes	yes	yes
Au/Cr 4	3	yes	yes	yes

Table 4: The individual devices fabricated and measured are given in the table. All devices were fabricated via laser writer, except the ones labelled with EB with electron-beam lithography.

One key motivation for achieving phase-sensitive amplification is its ability to generate squeezed coherent states. Such states are of big relevance for reducing the signal-to-noise ratio (SNR) in microwave measurements, hence improving measurement sensitivity and overall system performance [79, 80].
The presence of noisy phase spectra in combination with HONL may indicate further limitations in the achievable phase sensitivity. A detailed analysis of the underlying mechanisms is beyond the scope of this work.

Key Message

- The PA mechanism deviates from Lorentzian behaviour and is non-linear:
  1. Double peaked "Lorentzian" $\rightarrow$ noisy phase traces observed.
  2. Single peak $\rightarrow$ no noisy phase trace.

[15] The noisy phase trace is not consistently observed, but seems to depend on applied DC bias and P_p.

4.4 Material comparison - Reflection

This subsection presents a comparative analysis of the reflection measurements for all investigated electrode stacks. It serves as the analogue to chapter 4.3, but focusing on the reflection data introduced in chapter 4.1.

4.4.1 Capacitance Voltage Curve

The capacitance of the varactor is the variable component in the QPPA and hence the key driving parameter for PA. Fig. 17 (Au/Cr 2), 33a (Au/Ti 2), and 33b (Au 1(EBL)) show the capacitance-voltage (CV) characteristics for the different electrode stacks. Out of all the investigated devices the Au/Cr devices (Fig. 17) consistently show the highest zero-field capacitance C_0, the steepest CV slope, and strong reduction in C_0/C_{return} after exposure to voltages up to 5 V. These are followed by Au/Ti (Fig. 33a), which show slightly lower capacitance and tunability reduction.
For Au devices C_0 and C tunability is lowest and C_0/C_{return} is least influenced by voltage exposure. If they are fabricated by electron beam lithography (Fig. 33b), a slight C_0/C_{return} reduction is observed. In contrast, if fabricated by laser-writer, they show nearly constant initial capacitance and C_0/C_{return} (= 99%). The C_0/C_{return} of all investigated devices is summarised

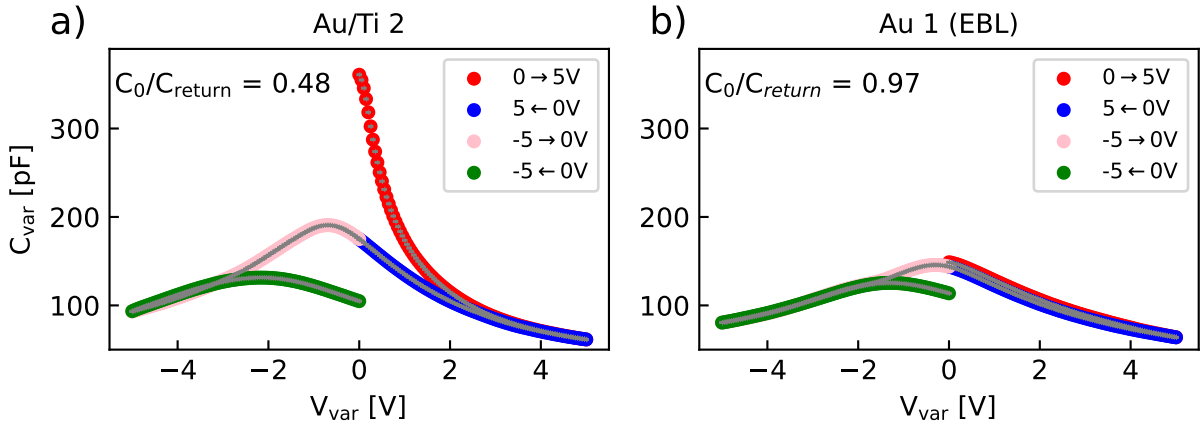

Figure 33: The capacitance as a function of voltage applied to the varactor is shown for Au/Ti 2 in **a** and Au 1 (EBL) in **b**.

in Fig. 34. A clear correlation between tunability reduction and PA performance is observed. Devices Au 1,2, fabricated with photolithography, exhibited no reduction in C_0/C_{return} and also no measurable parametric gain. In contrast, Au devices fabricated by E-beam lithography exhibited a slight reduction in C_0/C_{return} and showed good PA performance only during the first cool-down.
The remaining devices, Au/Ti and Au/Cr, both fabricated with photolithography, exhibited a significant reduction in C_0/C_{return} and consistently showed strong, reproducible PA. These observations indicate that reduced C_0/C_{return}, associated with interfacial states, material defects like oxygen vacancies, and especially trapped charges, appear to be desired for PA operation [45, 49, 52, 74–76].
The trend shows that a decrease in C_0/C_{return} is associated with a device being able to achieve high PA. Therefore, PA performance was examined in the negative bias region, where C_0/C_{return} is even more reduced after voltage exposure. However, the gain in this region was significantly lower than that observed under positive bias.

Experimentally, in [38], it was observed that at Au/STO interfaces oxygen vacancies are significantly promoted and even thermodynamically migrate to the interface. This potentially shields the STO from being exposed to an external electric field, reducing the capacitance tunability, hence effective PA.

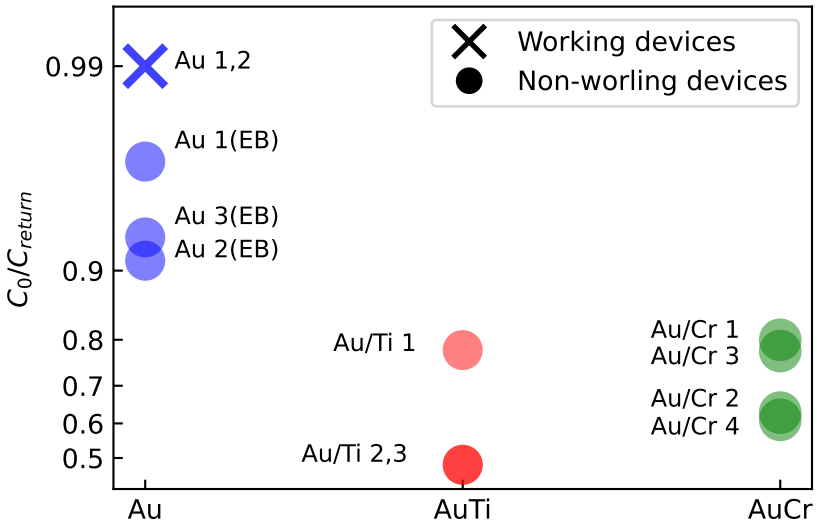

Figure 34: The capacitance decrease of the varactor after 5 V exposure (C_0/C_{return}) is shown for the different electrode stacks. Circular symbols represent devices capable of achieving high gain, whereas x-shaped symbols represent those that are not.

Key Message

- Au devices are unreliable and produce inconsistent measurement data.
- Au devices only show PA, if fabricated via electron-beam lithography due to charge defects.
- If the C_0/C_{return} decreases after voltage exposure, the device achieves good PA performance. Hence, hysteresis due to material defects, trapped charges and oxygen vacancies is desired.
- In the negative bias regions, C_0/C_{return} is lowest. However, the gain is significantly smaller than in the positive bias region.

4.4.2 Loss tangent $\tan(\delta)$

The loss tangent measured for all the devices during this work are higher than the experimentally achieved loss tangent, $\tan(\delta) = 0.005$ with superconducting electrodes[45]. Though it can be seen, that for using no sticking layer (Fig. 35b) the $\tan(\delta)$ is lowest, followed by Au/Ti (35a), and Au/Cr (Fig. 18b) having the highest $\tan(\delta)$ values. This trend is consistently observed for all devices, and more prominently seen for increasing V_{var} .
For the Au/Ti 1 device local heating was observed for $P_p \geq 24\,dBm$, when measuring in the VTI (see chap. 4.6). In future works, one could investigate the correlation between $\tan(\delta)$ and local heating for the different materials as a function of P_p, to make the devices more microkelvin compatible.

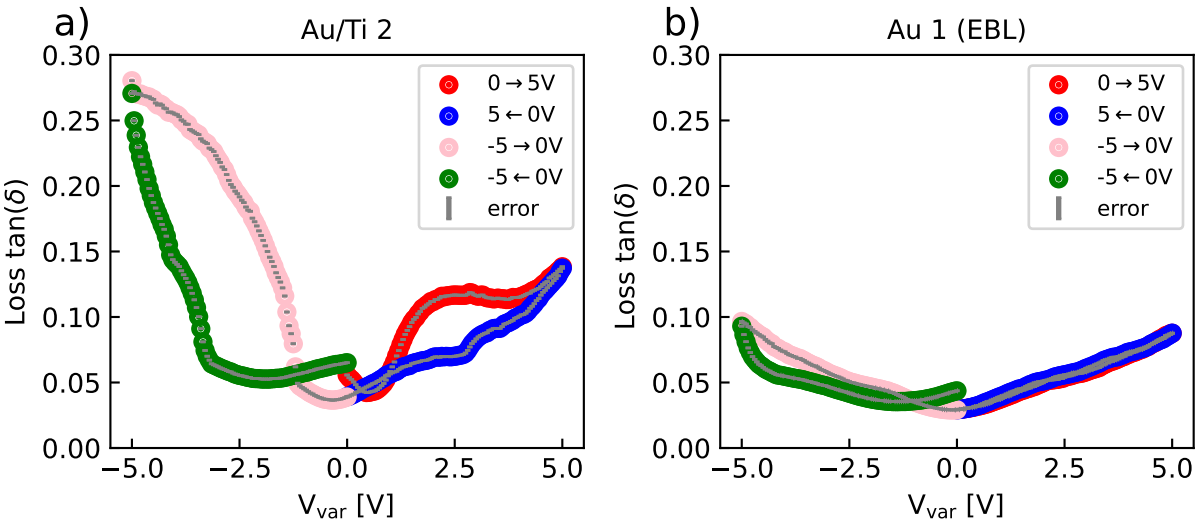

Figure 35: The loss tangent as a function of the DC bias is shown for Au/Ti 2 in **a)** and Au 1 (EBL) in **b)**.

Key Message

- $\tan(\delta)_{Au/Cr} > \tan(\delta)_{Au/Ti} > \tan(\delta)_{Au}$
- Local heating up to 9 K observed for $P_p \geq 24$ dBm, but it did not affect the gain.

.

4.4.3 Material Trends

This chapter presents scatter plots to identify trends and correlations between the different devices. Each dot represents a specific V_{var} , where the device was measured at (range 0 up to 2 V, from lighter to darker colour transition.). The y-axis represents the P_p required to achieve $G_{nd} = 20$ dB[16]. In Fig. 36a, the x-axis is the derivative value at a given V_{var} [17]. Au needs the most P_p to achieve 20 dB gain. For Au/Ti and Au/Cr, the P_p required has a broader range, with Au/Cr indicating a lower P_p at optimum V_{var}. The plot shows that for a smaller varactor gap size a steeper CV slope and larger C_0 makes the device able to achieve equal gain for lower P_p at an ideal V_{var} , because the C_{var} achieves larger oscillations without reaching into the negative bias region as fast (see Fig 5).

In Fig. 36b the x-axis is the Q-factor[18]. The Q-factor appears to be optimal at Q = 20 for Au/Cr devices, if device Au/Cr 4 is excluded. The reason for the Au/Cr 4 Q-factor being much more tunable is not known, but it could be due to fewer charge defects, leading to less shielding of STO from external E-fields. It also becomes clear that the Q-factor decreases with increasing V_{var} because of higher resistive losses (the loss tangent increases as V_{var} rises)[59]. Furthermore, for higher P_p, local heating causes additional dissipation in all devices. The importance of varactor tunability becomes clear when looking at the Au/Cr 3 device. The P_p range required to achieve 20 dB gain is very narrow and behaves almost like a fixed value

[16]The y-axis was investigated for G_{nd} and G_d = 10 and 20 dB. Trend stayed the same for all of them.
[17]For an example, see Fig. 18a
[18]For an example, see Fig. 24.

component. This behaviour arises from using a cross-shaped rather than circular geometry for the inner varactor ring (Appendix Fig. 45), which reduces the capacitance tunability. There is some discrepancy in the stated trends, which have to be further investigated.
The next step would be to significantly reduce the P_p required to achieve high gain. By introducing superconducting electrodes much higher Q-factors may be achieved.

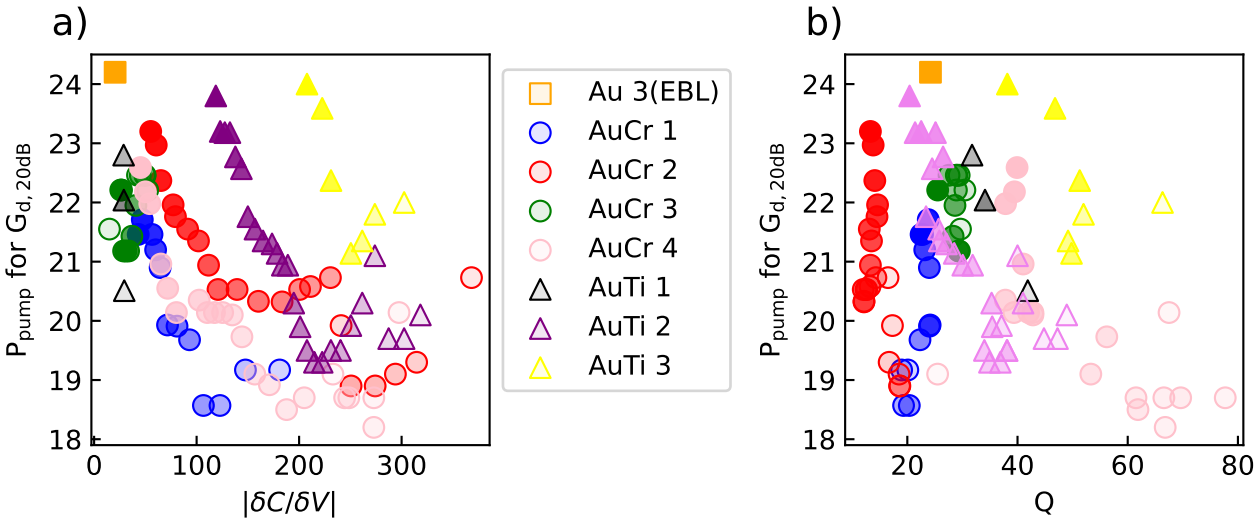

Figure 36: The pump power required to achieve $G_d = 20\,dB$ is presented as a function of the corresponding capacitance derivative value (example Fig. 18) in **a)** and the Q-factor in **b)** at a given voltage bias for each dot.

Key Message

- Reducing the varactor gap size improves the capacitance modulation achieved per unit RF $P_p \rightarrow$ Less P_p requiered for equal amount of gain.
- The Q-factor reduces for increasing V_{var} and $P_p \rightarrow$ more P_p required for equal gain due to increased $\tan(\delta)$, local heating and energy dissipation.
- The Q-factor is not very tunable for majority of the devices, apart from devices Au/Cr 4 and Au/Ti 3.

4.5 Dependence on Inductor

This chapter discusses how the operational frequency range of the Au/Cr 4 device can be increased by reducing the inductor L_1 (see the circuit in Fig. 9). Figure 37 illustrates the influence of L_1 for values of 12.1 nH, 8.9 nH, and 5.5 nH. Taking $L_1 = 12.1\,nH$ as the reference, a decrease to 8.9 nH should theoretically increase the resonance frequency by 16%, and a reduction to 5.5 nH by 48%[19]. Experimentally, however, the observed frequency shifts are only $\approx 4\%$ and $\approx 14\%$. This discrepancy potentially indicates that parasitic inductance, together with the bondwire inductance, contribute significantly in addition to L_1, thereby limiting the achievable shift in f_{res}. To investigate whether the efficiency of the f_{res} tuning can be improved, the loop height should be reduced and the bondwire length minimized. Alternatively, the STO crystal thickness could be reduced by introducing a parallel capacitor to achieve higher frequencies.

[19]These theoretical shifts are obtained from the expression $1/2\pi\sqrt{LC} \leftrightarrow \sqrt{L_1}/\sqrt{L_2}$.

However, this would complicate the integration into the PCB.
The higher the operating frequency range, the better the impedance has to be matched to significantly minimize losses.

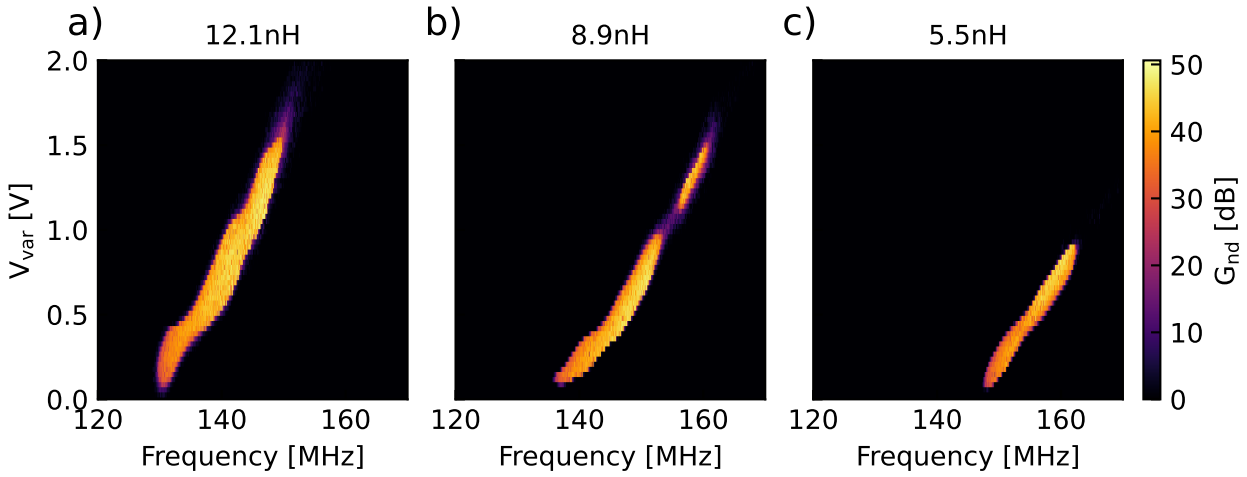

Figure 37: The influence of the inductor L_1 on the frequency range of operation for PA is shown for the Au/Cr 4 device. Panel **a)**, **b)**, and **c)** correspond to inductance values of 12.1 nH, 8.9 nH, and 5.5 nH. The gain as a function of voltage is presented for the Au/Cr 4 device. The pump power was set to $P_p = 25$ dBm. The signal frequency f_s was fixed at half the pump frequency f_p, while both frequencies were swept simultaneously.

Key Message

- Parasitic and bondwire inductance have a significant impact on the QPPA f_{res} and significantly reduce the f_{res} tunability of the device for higher frequencies.

4.6 Magnetic field dependence

The following measurements were conducted at ≈ 1.6 K to investigate the magnetic field dependence of the Au/Ti 1 device (see setup in Appendix Fig. 44). Fig. 38a shows the B-field dependent gain of the AuTi 1 device at $V_{var} = 0.42$ V. As the B-field increases, the f_{res} shifts to higher frequency, following a non-linear relation with B. The gain stays stable, independent of B, but the P_p required increases slightly with increasing B.
Interestingly, f_{res} exhibits irreversible polarisation. After exposing the device to 1 T and then reducing the field back to 0 T, f_{res} remains at the value it had at 1 T. Analogously, when exposed to 5 T. This irreversible behaviour may be caused by a nearby screw used to fix the PCB onto the VTI insert, the aluminium bond-wire used to DC bias the varactors, or a combination of both. For pumping over 25 dBm, local heating up to 9 K was observed, but it had no impact on the gain.
Fig. 38b shows that, at a given B-field the f_{res} does not shift. The gain remains stable across the entire range, here from -5 to 5 T.

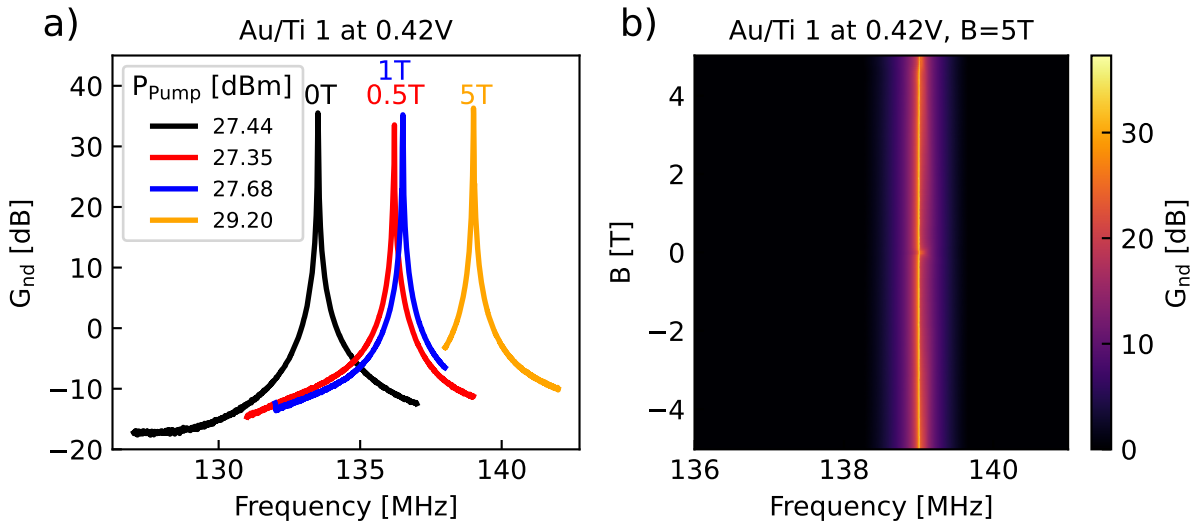

Figure 38: **a)** The non-degenerate gain as a function of frequency is shown for various external magnetic fields. **b)** The non-degenerate gain and f_{res} stays stable from 5 to -5 T.

4.7 Varactor Gap Size Influence

Figure 39 presents the operational frequency ranges of the Au/Ti 2 (gap size $\approx 1\,\mu$m) and Au/Ti 3 (gap size $\approx 5\,\mu$m) varactors. The Au/Ti 2 device exhibits a tunable band from 115 to 151 MHz, while the Au/Ti 3 device operates over a narrower 130–145 MHz range. The main takeaway is that decreasing the gap size enhances the overall capacitance tunability and broadens the usable frequency range for PA under DC bias. Additionally, it improves the capacitance modulation achieved per unit RF pump power. As a result, equal gain requires less P_p (see Fig. 36).

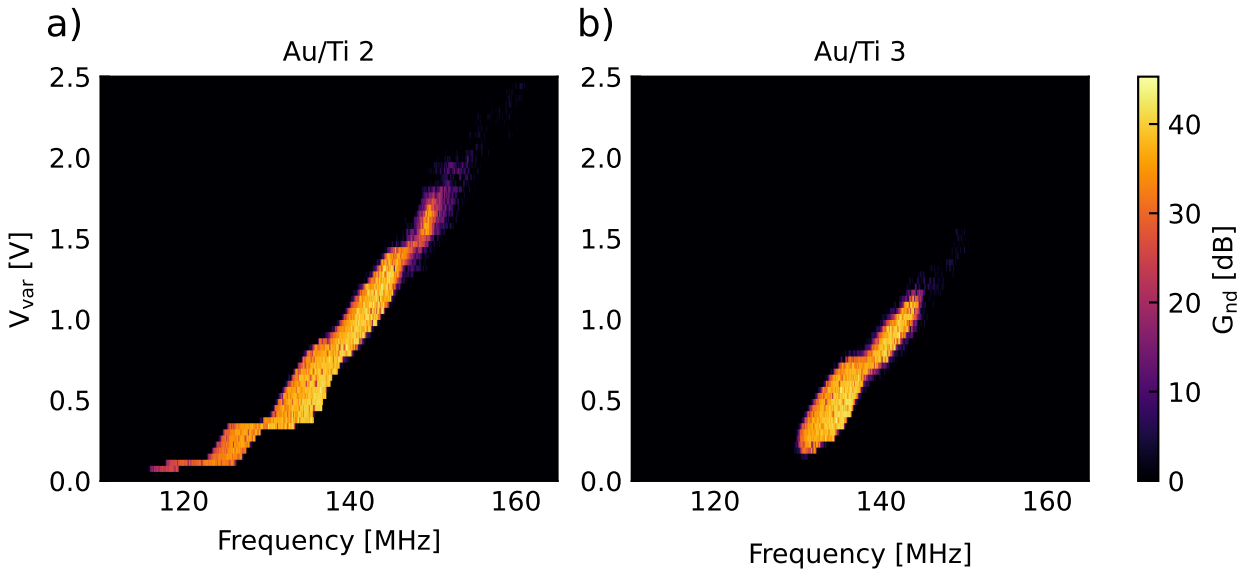

Figure 39: The gain as a function of voltage is shown for Au/Ti 2 and 3. Here, the pump power was set to P_p=25 dBm. The f_s was fixed to half of f_p and both frequencies were simultaneously swept. The measurements were done on Au/Ti 2 and 3 with a varactor gap size of 1 μm in **a)** and 5 μm for **b)**.

4.7.1 Anomalies

It is widely know, that the hysteretic behaviour of the capacitance of STO, originating from an applied DC bias, can be reversed by thermally heating it up to room temperature [45, 49–51]. However, an effect that is not yet understood was observed, as neither thermal resetting at room temperature for up to 1 h nor heating the device with a heat gun at 350 °C with low airflow for 1-3 min restores the initial f_{res} measured after the first cool down (Fig. 40).

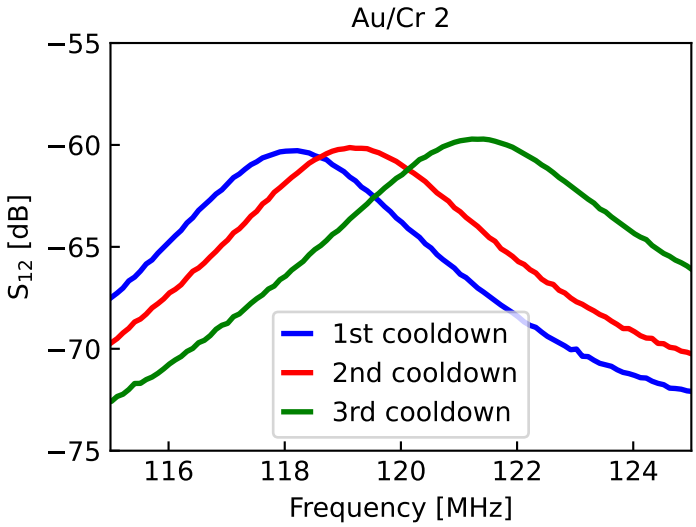

Figure 40: The initial f_{res} of the Au/Cr 2 (LW) device is depicted for the first time cooling down to 4.2 K in blue and then after thermally reheating the device at RT for 1h cooling it down again in red and analogously a third time in green.

The slight shift (1-5 MHz) may explain why Au 1,3 (EBL) devices only worked during the first cool-down, where the amount of trapped charges and shielding was negligible. For Au/Cr and Au/Ti devices a 2-5 MHz increase in f_{res} was also observed, but the impact was minimal, as the gain remained identical. The PA performance remained consistent. But the frequency range at the high and low ends of the spectrum was slightly reduced and the overall response became smoother and more stable, as shown in Fig. 41. This DC bias history was not investigated actively for this type of measurement in Fig. 41, hence this is the only device measured twice for PA.

Additionally, in some cases, the coupling capacitors were damaged due to excessive pump power. This resulted in reduced gain or, in certain cases, a non-functional device that had initially worked. Such capacitor failures were consistently observed in Au-based devices. Replacing the affected capacitors restored device functionality for Au/Cr and Au/Ti devices, but not for Au devices.

For Au devices, the coupling capacitors (C_c) appeared to fail more easily. In the present experiments, a maximum DC bias of 5 V and a P_p of 25 dBm (corresponding to $P_{pp} \approx 11.24$ V) were applied.When considering the high gain, it can be said that P_p was increased gradually, to prevent dielectric breakdown and burning of the capacitors, which did not help.

Furthermore, the performance of Au devices appears to be unstable or unreliable based on the available data. Multiple Au devices were tested, and after the first operation, the gain did not recover to its initially high values, even after replacing the coupling capacitors.

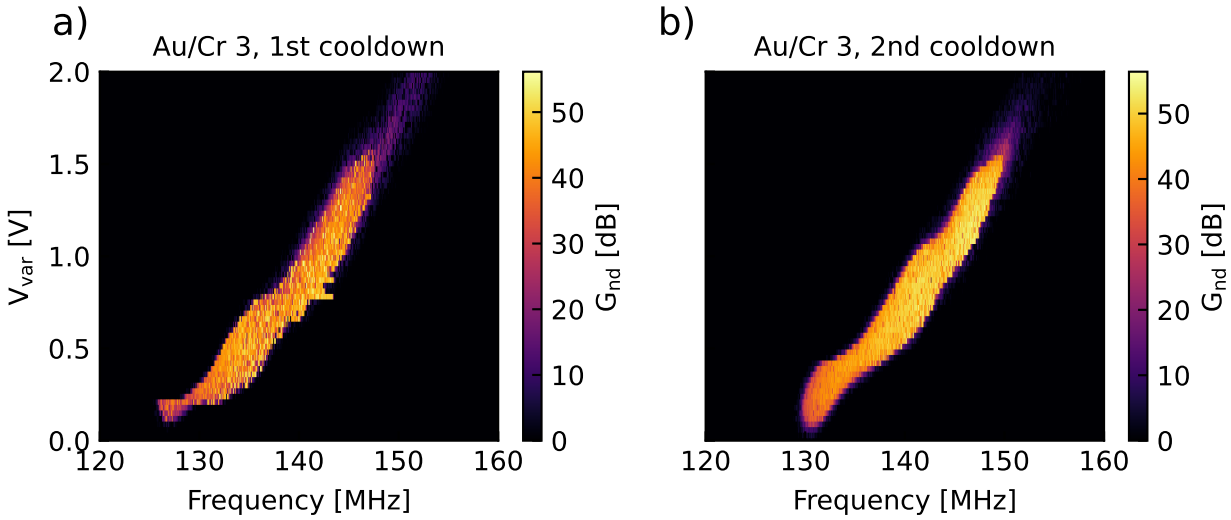

Figure 41: Influence of DC bias history on the measurements: **a)** after the first cooldown with no prior applied DC bias, and **b)** after the second cooldown following a DC bias history up to $V_{var} = 3\,V$. The f_s was fixed to half of f_p and both frequencies were simultaneously swept.

Key Message

- The QPPA is B-field independent from -5 T to 5 T, but irreversible polarisation takes place at 1.6 K temperature.
- Increasing the B-field requires increasing P_p for equal gain.
- The smaller the varactor gap size, the wider the frequency range, in which the QPPA can achieve high gain parametric amplification.
- Local heating up to 9 K was observed for $P_p \geq 25\,dBm$, but the gain was not affected.
- A thermally non-reversible f_{res} shift is observed for applied DC bias, which causes an increasing initial f_{res} per cool down.

5 Conclusion And Outlook

This thesis presents a systematic investigation of STO varactors based quantum parametric paraelectric amplifier (QPPA) circuits. The focus was on how different electrode stacks, with and without adhesion layers, influence the non-linear dynamics and amplification performance. By combining theoretical models with experimental results, a deeper understanding of the system was achieved.

The results confirm STO to be a suitable material for parametric amplification at cryogenic temperatures due to its dielectric constant being strongly dependent on an external electric field. This allows capacitance modulation and three-wave mixing. However, the performance of the device is not only determined by the non-linearity of STO, but also by its external effects, such as interface configuration and defects.

A key finding is that Cr and Ti adhesion layers significantly influence device performance compared to devices without an adhesion layer. The adhesion layers enhance the mechanical

stability of the gold overlayer. They also alter the STO response via interdiffusion and defect generation. Consequently, Au/Cr and Au/Ti devices exhibit higher zero-field capacitance, greater capacitance tunability, and a reduction in capacitance following voltage exposure (hysteresis). Based on the results, the increased hysteresis introduced by the adhesion layer is desired, as it strongly indicates that a device can achieve high gain. Nonetheless, similar gain can be achieved, independent of electrode stack, by adjusting the pump power.
QPPA devices without a sticking layer suffer from peeling and delamination. They also yield irreproducible results and exhibit no gain after the initial cooldown.
Beyond material effects, the non-linear dynamics such as the Duffing non-linearity and non-linear damping play an important role at higher pump powers. They modify the resonance frequency condition and peak shape, gain saturation, and amplifier stability. Also the phase sensitivity is significantly reduced at high pump powers.
The operational frequency range for high-gain parametric amplification increases as the varactor gap is reduced. However, when trying to reach higher frequencies by reducing the inductance of the LC resonator the achievable shift is limited by parasitic and bondwire inductance.
The QPPA achieves high gain at a fixed resonance frequency independent of a magnetic field from -5 T to 5 T, however, an irreversible polarisation is observed.
The current devices exhibit inconsistencies in Q-factor tunability. Additionally, resetting the polarization of STO via thermal heating at RT leads to a slight shift to higher resonance frequency compared to initial values. This is likely due to the fabrication induced defects and has to be investigated.
The pump power needed to achieve high gain is very high. One proposal to address this challenge is to try to use thin film superconducting electrodes, which potentially increase the Q-factor significantly, lowering the required pump power, hence decrease the noise, energy dissipation, and heating. An asymmetric coupling capacitor circuit configuration may achieve similar effects. This may allow to work below the cryogenic temperature noise floor and even make the QPPA microkelvin compatible. However, the fabrication recipe has to be reinvented to actively control external effects on the STO.
Additionally, when trying to reach higher frequencies, the device is limited by bondwire and parasitic capacitance. Reducing bondwire length or reducing the thickness of STO should theoretically provide a pathway to higher frequencies.
Lastly, one could fabricate Au/Cr and Au/Ti devices with EBL, to push for smaller varactor gap sizes, to see if they further increase the amplifier performance.

6 Acknowledgment

I want to thank **Prof. Dr. Dominik Zumbühl** for giving me the opportunity last year to join his research group to conduct both my master project and this master thesis. His supervision and open mindedness allowed me to work very independently, while keeping me on the right track. The time in his group allowed me to grow as a scientist and gave me the opportunity to meet great people due to the groups warm and supportive environment. I am also very grateful to Dominik for inviting me to the second MolQ meeting in Meiersalp and for the opportunity to present my work in the upcoming NCCR Spin annual meeting 2026 in Pontresina.

I thank **Henok Weldeyesus** for giving me valuable input on how to work more efficiently as a scientist and for the fruitful discussions.

Also thanks to **Dr. Aldo Tarascio** for fabricating the devices and giving me valuable input on the nano-fabrication.

A big thanks goes to **Dr. Rafael Eggli**. He supervised me during both my masters project and this thesis. His guidance and patience allowed me to learn by doing things myself. As i encountered obstacles, his expertise and thoughtful input gave me valuable perspectives on how to face challenges and overcome them. I am sincerely grateful for his support and for helping me grow as a physicist. I do not take your trust in me for granted and could have not wished for a better supervisor.

Lastly, i want to thank my **Mom**. Everything i have achieved is thanks to you. Because of you and for you.

என் அன்பு அம்மாவுக்கு நன்றி கூற விரும்புகிறேன். நான் அடைந்த எல்லா சாதனைகளும் உங்களால்தான்.

References

[1] A. Janzen and S. Weinreb, "Manufacturable cryogenic SiGe LNA for radio astronomy and space communications", 1–2 (2016).

[2] F. Hudelist, J. Kong, C. Liu, J. Jing, Z. Ou, and W. Zhang, "Quantum metrology with parametric amplifier-based photon correlation interferometers", Nature Communications **5**, 10.1038/ncomms4049 (2014).

[3] R. Lasenby, "Parametrics of electromagnetic searches for axion dark matter", Physical Review D **103**, 075007 (2021).

[4] Y. Yu, "Advancements in Applications of Quantum Entanglement", Journal of Physics: Conference Series **2012**, 012113 (2021).

[5] F. Arute, K. Arya, R. Babbush, D. Bacon, J. C. Bardin, R. Barends, R. Biswas, S. Boixo, F. G. S. L. Brandao, D. A. Buell, B. Burkett, Y. Chen, Z. Chen, B. Chiaro, R. Collins, W. Courtney, A. Dunsworth, E. Farhi, B. Foxen, A. Fowler, C. Gidney, M. Giustina, R. Graff, K. Guerin, S. Habegger, M. P. Harrigan, M. J. Hartmann, A. Ho, M. Hoffmann, T. Huang, T. S. Humble, S. V. Isakov, E. Jeffrey, Z. Jiang, D. Kafri, K. Kechedzhi, J. Kelly, P. V. Klimov, S. Knysh, A. Korotkov, F. Kostritsa, D. Landhuis, M. Lindmark, E. Lucero, D. Lyakh, S. Mandrà, J. R. McClean, M. McEwen, A. Megrant, X. Mi, K. Michielsen, M. Mohseni, J. Mutus, O. Naaman, M. Neeley, C. Neill, M. Y. Niu, E. Ostby, A. Petukhov, J. C. Platt, C. Quintana, E. G. Rieffel, P. Roushan, N. C. Rubin, D. Sank, K. J. Satzinger, V. Smelyanskiy, K. J. Sung, M. D. Trevithick, A. Vainsencher, B. Villalonga, T. White, Z. J. Yao, P. Yeh, A. Zalcman, H. Neven, and J. M. Martinis, "Quantum supremacy using a programmable superconducting processor", Nature **574**, 505–510 (2019).

[6] L. M. Gächter, R. Garreis, J. D. Gerber, M. J. Ruckriegel, C. Tong, B. Kratochwil, F. K. de Vries, A. Kurzmann, K. Watanabe, T. Taniguchi, T. Ihn, K. Ensslin, and W. W. Huang, "Single-Shot Spin Readout in Graphene Quantum Dots", PRX Quantum **3**, 020343 (2022).

[7] D. P. DiVincenzo, "The Physical Implementation of Quantum Computation", Fortschritte der Physik **48**, 771–783 (2000).

[8] A. E. Kass, C. T. Jin, J. D. Watson, G. C. Gardner, S. Fallahi, M. J. Manfra, and D. J. Reilly, "An rf Quantum Capacitance Parametric Amplifier", 10.48550/ARXIV.2304.13227 (2023).

[9] A. A. Clerk, M. H. Devoret, S. M. Girvin, F. Marquardt, and R. J. Schoelkopf, "Introduction to quantum noise, measurement, and amplification", Reviews of Modern Physics **82**, 1155–1208 (2010).

[10] B. Mohammadian, "Superconducting Parametric Amplifiers: Resonator Design and Role in Qubit Readout", in *Perspectives on quantum technologies - modeling, simulation, and implementation*, edited by E. Sakk (IntechOpen, London, 2025) Chap. 5.

[11] N. Klimovich, P. Day, S. Shu, B. H. Eom, H. Leduc, and A. Beyer, "Demonstration of a Quantum Noise Limited Traveling-Wave Parametric Amplifier", 10.48550/ARXIV.2306.11028 (2023).

[12] M. Esposito, A. Ranadive, L. Planat, and N. Roch, "Perspective on traveling wave microwave parametric amplifiers", Applied Physics Letters **119**, 10.1063/5.0064892 (2021).

[13] S. Lulinsky, B. Torteman, B. R. Ilic, and S. Krylov, "Parametric Amplification of Acoustically Actuated Micro Beams Using Fringing Electrostatic Fields", Micromachines **15**, 257 (2024).

[14] D. Li and S. W. Shaw, "The effects of nonlinear damping on degenerate parametric amplification", Nonlinear Dynamics **102**, 2433–2452 (2020).

[15] C. M. Caves, J. Combes, Z. Jiang, and S. Pandey, "Quantum limits on phase-preserving linear amplifiers", Physical Review A **86**, 063802 (2012).

[16] D. A. Trüssel, "A Quantum Paraelectric Parametric Amplifier", Msc thesis (University of Basel, 2025).

[17] K. Sivasubramaniam, "Achieving High Gain in a Parametric Amplifier Based on SrTiO3 Varactors", Msc project (University of Basel, 2025).

[18] R. C. Neville, B. Hoeneisen, and C. A. Mead, "Permittivity of Strontium Titanate", Journal of Applied Physics **43**, 2124–2131 (1972).

[19] C. Ang, A. S. Bhalla, and L. E. Cross, "Dielectric behavior of paraelectric $KTaO_3$, $CaTiO_3$, and $(Ln_{1/2}Na_{1/2})TiO_3$ under a dc electric field", Physical Review B **64**, 184104 (2001).

[20] R. W. Boyd, "The nonlinear optical susceptibility", in *Nonlinear optics* (Elsevier, 2020), pp. 1–64.

[21] R. Eggli, "Gate-Reflectometry with Hole Spins", PhD thesis (University of Basel, 2025).

[22] A. Eichler and O. Zilberberg, "The Harmonic Resonator", in *Classical and quantum parametric phenomena* (Oxford University PressOxford, Sept. 2023), pp. 5–19.

[23] A. Eichler and O. Zilberberg, "The Duffing Resonator", in *Classical and quantum parametric phenomena* (Oxford University PressOxford, Sept. 2023), pp. 20–31.

[24] R. H. Rand, *Lecture Notes on Nonlinear Vibrations*, Version 53, Ithaca, NY, USA, 2012.

[25] M. Krack and J. Gross, *Harmonic balance for nonlinear vibration problems*, Mathematical Engineering (Springer International Publishing, 2019).

[26] H. G. Schuster, ed., *Reviews of nonlinear dynamics and complexity*, Vol. 1 (Wiley-VCH, Weinheim, 2008).

[27] A. Eichler, J. Chaste, J. Moser, and A. Bachtold, "Parametric Amplification and Self-Oscillation in a Nanotube Mechanical Resonator", Nano Letters **11**, 2699–2703 (2011).

[28] A. Leuch, L. Papariello, O. Zilberberg, C. L. Degen, R. Chitra, and A. Eichler, "Parametric Symmetry Breaking in a Nonlinear Resonator", Physical Review Letters **117**, 214101 (2016).

[29] S. Neumeyer, V. Sorokin, M. van Gastel, and J. Thomsen, "Frequency detuning effects for a parametric amplifier", Journal of Sound and Vibration **445**, 77–87 (2019).

[30] D. M. Pozar, *Microwave engineering*, Fourth edition, Enthält Übungsaufgaben (John Wiley & Sons, Inc., Hoboken, NJ, 2012), 1732 pp.

[31] S. Arar, *Using the 1 dB Compression Point to Characterize RF System Nonlinearity*, All About Circuits, (May 18, 2025) `https://www.allaboutcircuits.com/technical-articles/using-the-1-db-compression-point-to-characterize-rf-system-nonlinearity/` (visited on 03/10/2026).

[32] J. J. Carr, *RF components and circuits*, 1. ed., reprint, Includes bibliographical references and index (Newnes, Oxford [u.a.], 2005), 398 pp.

[33] M. Steer, ed., *Microwave and RF Design, Volume 4 : modules*, Open textbook library (North Carolina State University Libraries, Raleigh, North Carolina, 2019), 1 p.

[34] M. A. El-Hiti, M. A. Ahmed, and M. El-Shabasy, "Electrical properties of thin chromium films", Journal of Materials Science Letters **8**, 329–333 (1989).

[35] E. Acosta, "Thin Films/Properties and Applications", in *Thin films* (IntechOpen, Nov. 2021).

[36] M. RaeisianAsl, S. Jouybar, S. Sarabadani Tafreshi, and L. Naji, "Exploring the key features for enhanced $SrTiO_3$ functionality: A comprehensive overview", Materials Today Sustainability **29**, 101072 (2025).

[37] D. Shin, S. Latini, C. Schäfer, S. A. Sato, U. De Giovannini, H. Hübener, and A. Rubio, "Quantum paraelectric phase of $SrTiO_3$ from first principles", Physical Review B **104**, l060103 (2021).

[38] X. Ma, Y. Dai, M. Li, and B. Huang, "Oxygen vacancies at the Au/$SrTiO_3$(001) interface: stabilities, electronic properties and effect on photocatalysis", Physical Chemistry Chemical Physics **19**, 774–781 (2017).

[39] Y. Z. Ayino, "Superconductivity and Magnetism in Strontium Titanate Thin Films and Heterostructures", PhD thesis (FACULTY OF THE UNIVERISTY OF MINNESOTA, 2020).

[40] Y.-Y. Pai, A. Tylan-Tyler, P. Irvin, and J. Levy, "Physics of $SrTiO_3$-based heterostructures and nanostructures: a review", Reports on Progress in Physics **81**, 036503 (2018).

[41] A. Hallett, "First principles studies of thermal, structural, and chemical phase spaces in quantum materials", PhD thesis (University of California, Santa Barbara, 2024).

[42] E. McCalla, J. Walter, and C. Leighton, "A Unified View of the Substitution-Dependent Antiferrodistortive Phase Transition in $SrTiO_3$", Chemistry of Materials **28**, 7973–7981 (2016).

[43] K. Brahim, A. Boelen, A. Ulrich, M. Debaets, T. Tandecki, E. Mafakheri, C. Sun, Y. Huang, A. Potočnik, T. Ivanov, L. Nulens, J. Van de Vondel, C. Merckling, K. D. Greve, and C. Haffner, "Microwave permittivity and loss in epitaxial $SrTiO_3$", Applied Physics Letters **127**, 10.1063/5.0265424 (2025).

[44] K. A. Müller and H. Burkard, "$SrTiO_3$: An intrinsic quantum paraelectric below 4 K", Physical Review B **19**, 3593–3602 (1979).

[45] D. Davidovikj, N. Manca, H. S. J. van der Zant, A. D. Caviglia, and G. A. Steele, "Quantum paraelectricity probed by superconducting resonators", Physical Review B **95**, 214513 (2017).

[46] P. Zubko, S. Gariglio, M. Gabay, P. Ghosez, and J.-M. Triscone, "Interface Physics in Complex Oxide Heterostructures", Annual Review of Condensed Matter Physics **2**, 141–165 (2011).

[47] W. Kleemann, J. Dec, A. Tkach, and P. M. Vilarinho, "$SrTiO_3$—Glimpses of an Inexhaustible Source of Novel Solid State Phenomena", Condensed Matter **5**, 58 (2020).

[48] C. Ang and Z. Yu, "dc electric-field dependence of the dielectric constant in polar dielectrics: Multipolarization mechanism model", Physical Review B **69**, 174109 (2004).

[49] R. S. Eggli, S. Svab, T. Patlatiuk, D. A. Trüssel, M. J. Carballido, P. Chevalier Kwon, S. Geyer, A. Li, E. P. Bakkers, A. V. Kuhlmann, and D. M. Zumbühl, "Cryogenic hyperabrupt strontium titanate varactors for sensitive reflectometry of quantum dots", Physical Review Applied **20**, 054056 (2023).

[50] S. Gevorgian, A. Eriksson, A. Deleniv, and D. Pandey, "Double loop hysteresis in direct current dependent dielectric permittivity of $SrTiO_3$", Journal of Applied Physics **92**, 6165–6171 (2002).

[51] S. K. Ojha, S. Hazra, P. Mandal, R. K. Patel, S. Nigam, S. Kumar, and S. Middey, "Electron Trapping and Detrapping in an Oxide Two-Dimensional Electron Gas: The Role of Ferroelastic Twin Walls", Physical Review Applied **15**, 054008 (2021).

[52] C. Yin, A. E. M. Smink, I. Leermakers, L. M. K. Tang, N. Lebedev, U. Zeitler, W. G. van der Wiel, H. Hilgenkamp, and J. Aarts, "Electron Trapping Mechanism in $LaAlO_3/SrTiO_3$ Heterostructures", Physical Review Letters **124**, 017702 (2020).

[53] M. Gu, J. Wang, X. S. Wu, and G. P. Zhang, "Stabilities of the Intrinsic Defects on $SrTiO_3$ Surface and $SrTiO_3/LaAlO_3$ Interface", The Journal of Physical Chemistry C **116**, 24993–24998 (2012).

[54] A. Schiaffino and M. Stengel, "Macroscopic Polarization from Antiferrodistortive Cycloids in Ferroelastic $SrTiO_3$", Physical Review Letters **119**, 137601 (2017).

[55] Y. Frenkel, N. Haham, Y. Shperber, C. Bell, Y. Xie, Z. Chen, Y. Hikita, H. Y. Hwang, E. K. H. Salje, and B. Kalisky, "Imaging and tuning polarity at $SrTiO_3$ domain walls", Nature Materials **16**, 1203–1208 (2017).

[56] E. K. H. Salje, O. Aktas, M. A. Carpenter, V. V. Laguta, and J. F. Scott, "Domains within Domains and Walls within Walls: Evidence for Polar Domains in Cryogenic $SrTiO_3$", Physical Review Letters **111**, 247603 (2013).

[57] P. Zubko, G. Catalan, A. Buckley, P. R. L. Welche, and J. F. Scott, "Strain-Gradient-Induced Polarization in $SrTiO_3$ Single Crystals", Physical Review Letters **99**, 167601 (2007).

[58] M. Honig, J. A. Sulpizio, J. Drori, A. Joshua, E. Zeldov, and S. Ilani, "Local electrostatic imaging of striped domain order in $LaAlO_3/SrTiO_3$", Nature Materials **12**, 1112–1118 (2013).

[59] S. Gevorgian, *Ferroelectrics in Microwave Devices, Circuits and Systems, Physics, modeling, fabrication and measurements*, edited by A. Vorobiev and A. Deleniv, Engineering Materials and Processes Ser. Description based on publisher supplied metadata and other sources. (Springer London, Limited, London, 2009), 1411 pp.

[60] C. Corti and R. Holliday, eds., *Gold, Science and applications*, Formerly CIP Uk. - Includes bibliographical references and index (CRC Press, Boca Raton, Fla. [u.a.], 2010), 416 pp.

[61] B. Aghili, S. Rahbarpour, M. Berahman, and A. Horri, "Influence of Surface Roughness on the Work Function of Gold: A Density Functional Theory Study", The Journal of Physical Chemistry C **128**, 8077–8084 (2024).

[62] G. Mills, M. S. Gordon, and H. Metiu, "Oxygen adsorption on Au clusters and a rough Au(111) surface: The role of surface flatness, electron confinement, excess electrons, and band gap", The Journal of Chemical Physics **118**, 4198–4205 (2003).

[63] W. Bulowski, K. Skibińska, P. Żabiński, and M. Wojnicki, "Optimization of Gold Thin Films by DC Magnetron Sputtering: Structure, Morphology, and Conductivity", Coatings **15**, 1240 (2025).

[64] M. Hövel, B. Gompf, and M. Dressel, "Electrodynamics of ultrathin gold films at the insulator-to-metal transition", Thin Solid Films **519**, 2955–2958 (2011).

[65] T. Gilani and D. Rabchuk, "Electrical resistivity of gold thin film as a function of film thickness", Canadian Journal of Physics **96**, 272–274 (2018).

[66] D. J. J. J. R. Sambles K. C. Elsom, "The Electrical Resistivity of Gold Films", Philosophical Transactions of the Royal Society of London. Series A, Mathematical and Physical Sciences* **vol. 304**, pp. 365–396 (1981).

[67] R. Holliday and P. Goodman, "Going for gold [gold in electronics industry]", IEE Review **48**, 15–19 (2002).

[68] K. Zhao, D. Chen, and D. Li, "First principles study of interface structure and electronic property of $Au/SrTiO_3(001)$", Computational Materials Science **50**, 98–104 (2010).

[69] S. Jain, J. Bowers, M. Sysak, J. Heck, R. Feldesh, R. Jones, Y. Shetrit, and M. Geva, "Method of forming a semiconductor device including a gold layer", US9252118B2 (US) (T. S. M. Company, Feb. 2, 2016).

[70] M. Msimanga and M. McPherson, "Diffusion characteristics of gold in silicon and electrical properties of silicon diodes used for developing radiation-hard detectors", Materials Science and Engineering: B **127**, 47–54 (2006).

[71] W. M. Paulson and J. E. Hilliard, "Interdiffusion in composition-modulated copper-gold thin films", Journal of Applied Physics **48**, 2117–2123 (1977).

[72] J. Shields, C. R. d. Galarreta, J. Bertolotti, and C. D. Wright, "Enhanced Performance and Diffusion Robustness of Phase-Change Metasurfaces via a Hybrid Dielectric/Plasmonic Approach", Nanomaterials **11**, 525 (2021).

[73] C. Weaver and D. T. Parkinson, "Diffusion in gold-aluminium", Philosophical Magazine **22**, 377–389 (1970).

[74] M. Todeschini, A. Bastos da Silva Fanta, F. Jensen, J. B. Wagner, and A. Han, "Influence of Ti and Cr Adhesion Layers on Ultrathin Au Films", ACS Applied Materials & Interfaces **9**, 37374–37385 (2017).

[75] F. Corsetti and A. A. Mostofi, "Negative-U properties for substitutional Au in Si", EPL (Europhysics Letters) **105**, 57006 (2014).

[76] J. Ghatak, B. Sundaravel, K. G. M. Nair, and P. V. Satyam, "Ion-beam-induced enhanced diffusion from gold thin films in silicon", Journal of Physics: Condensed Matter **20**, 485008 (2008).

[77] J.-Y. Kim, M.-J. Jin, B. Hou, M. P. Kim, D.-S. Um, and C.-I. Kim, "Reducing the oxygen vacancy concentration in $SrTiO_3$-δ thin films via an optimized O_2 plasma treatment for enhancing device properties", Applied Surface Science **639**, 158271 (2023).

[78] C. Lin and A. A. Demkov, "Electron Correlation in Oxygen Vacancy in $SrTiO_3$", Physical Review Letters **111**, 217601 (2013).

[79] D. J. Parker, M. Savytskyi, W. Vine, A. Laucht, T. Duty, A. Morello, A. L. Grimsmo, and J. J. Pla, "Degenerate Parametric Amplification via Three-Wave Mixing Using Kinetic Inductance", Physical Review Applied **17**, 034064 (2022).

[80] L. Zhong, E. P. Menzel, R. Di Candia, P. Eder, M. Ihmig, A. Baust, M. Haeberlein, E. Hoffmann, K. Inomata, T. Yamamoto, Y. Nakamura, E. Solano, F. Deppe, A. Marx, and R. Gross, "Squeezing with a flux-driven Josephson parametric amplifier", New Journal of Physics **15**, 125013 (2013).

6 Appendix

6.1 Reflection And Transmission Setup

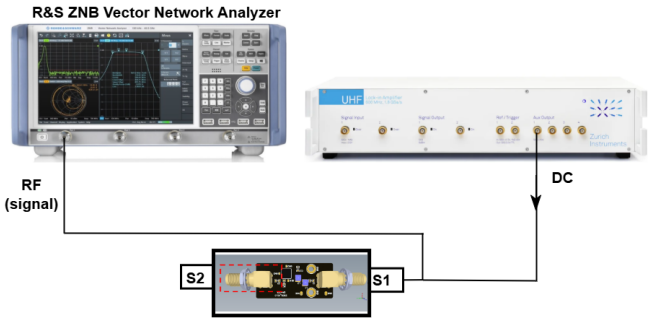

Figure 42: **Setup for reflection measurement inside a dewar at 4.2 K:** The vector network analyser sends an RF signal to the device and measures the S_{11} coefficient. The ultra-high frequency lock-in amplifier (UHFLI), from Zurich Instruments, DC biases the varactor.

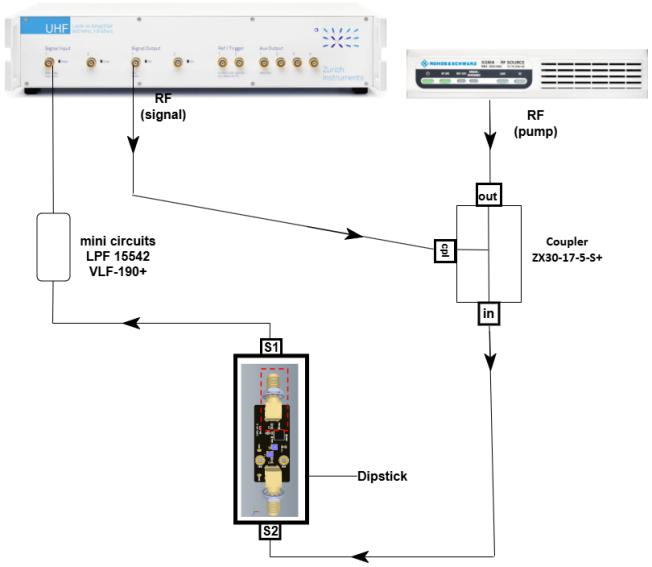

Figure 43: **Setup for transmission measurement inside a dewar at 4.2 K:** The SGS100A generates a RF pump tone of up to $P_p = 25\,\mathrm{dBm}$ and the UHFLI a RF signal tone additional to DC biasing the varactor. These signals are combined in the ZX30-17-5-s+ directional coupler and sent into the device. From the ports "out" $\rightarrow$ "in" 1 dBm and from "cpl" $\rightarrow$ "in" 16 dBm is lost. Then the amplified signal goes through a 300+ low-pass-filter and measures the S_{12} with the UHFLI.

6.2 Magnetic field Setup

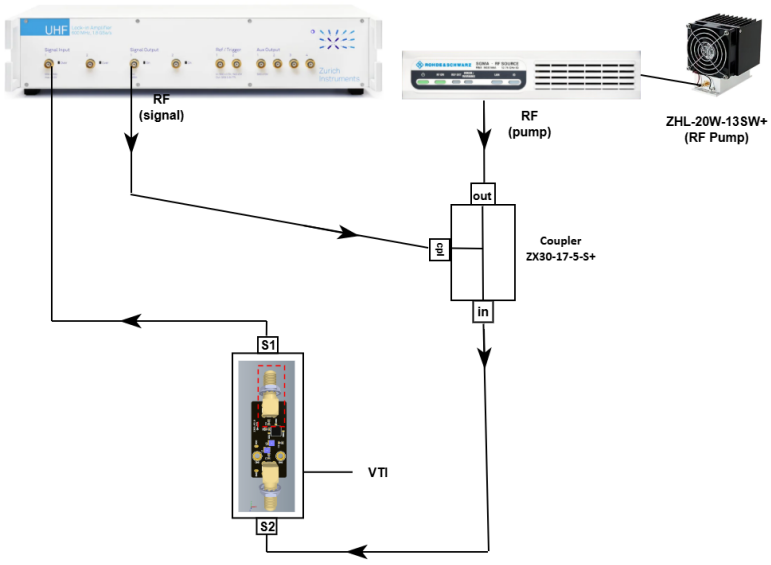

Figure 44: **Setup for transmission measurement inside a Variable temperature insert (VTI) at ≈1.6 K:Analogous to the setup in Fig.** 43, but here an additional RF pump source ZHL-20W-13SW+ is added to the Rhode Schwarz pump to achieve in total $P_p = 75\,dBm$.

6.3 Cross shaped Varactor

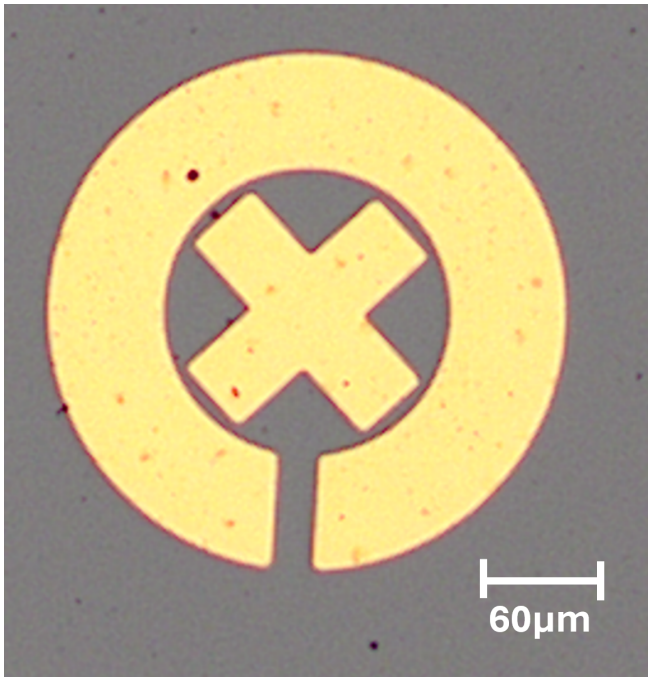

Figure 45: A light microscope image of the Au/Cr 3 device. The inner-ring is now cross-shaped and reduces the polarization tunability, hence the capacitance modulation.

6.4 1dB Compression Point

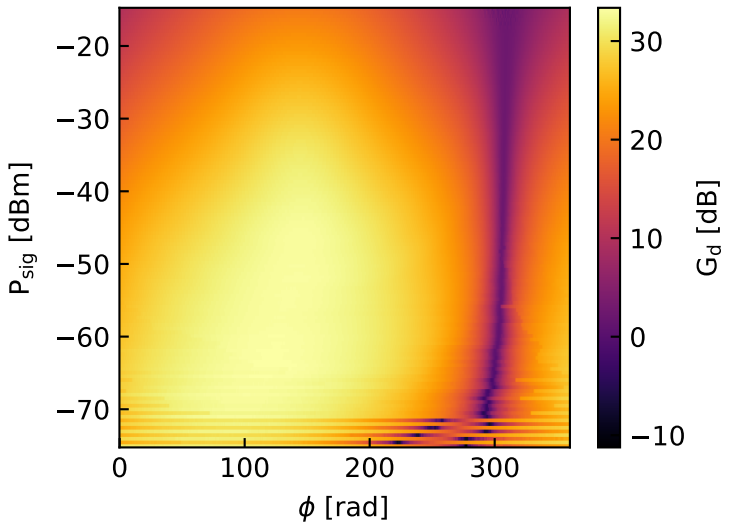

Figure 46: The input signal power as a function of the relative phase between signal and pump tone is shown.

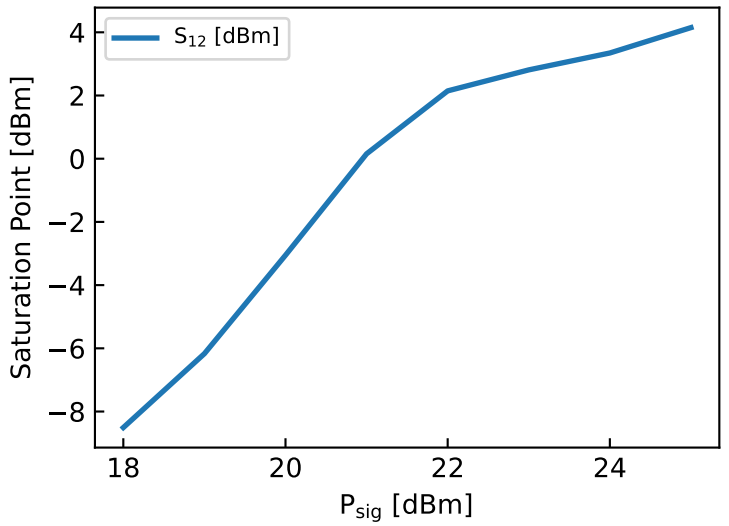

Figure 47: The saturation point for the different P_p at the kink in Fig. 25b as a function of P_{sig} is shown.

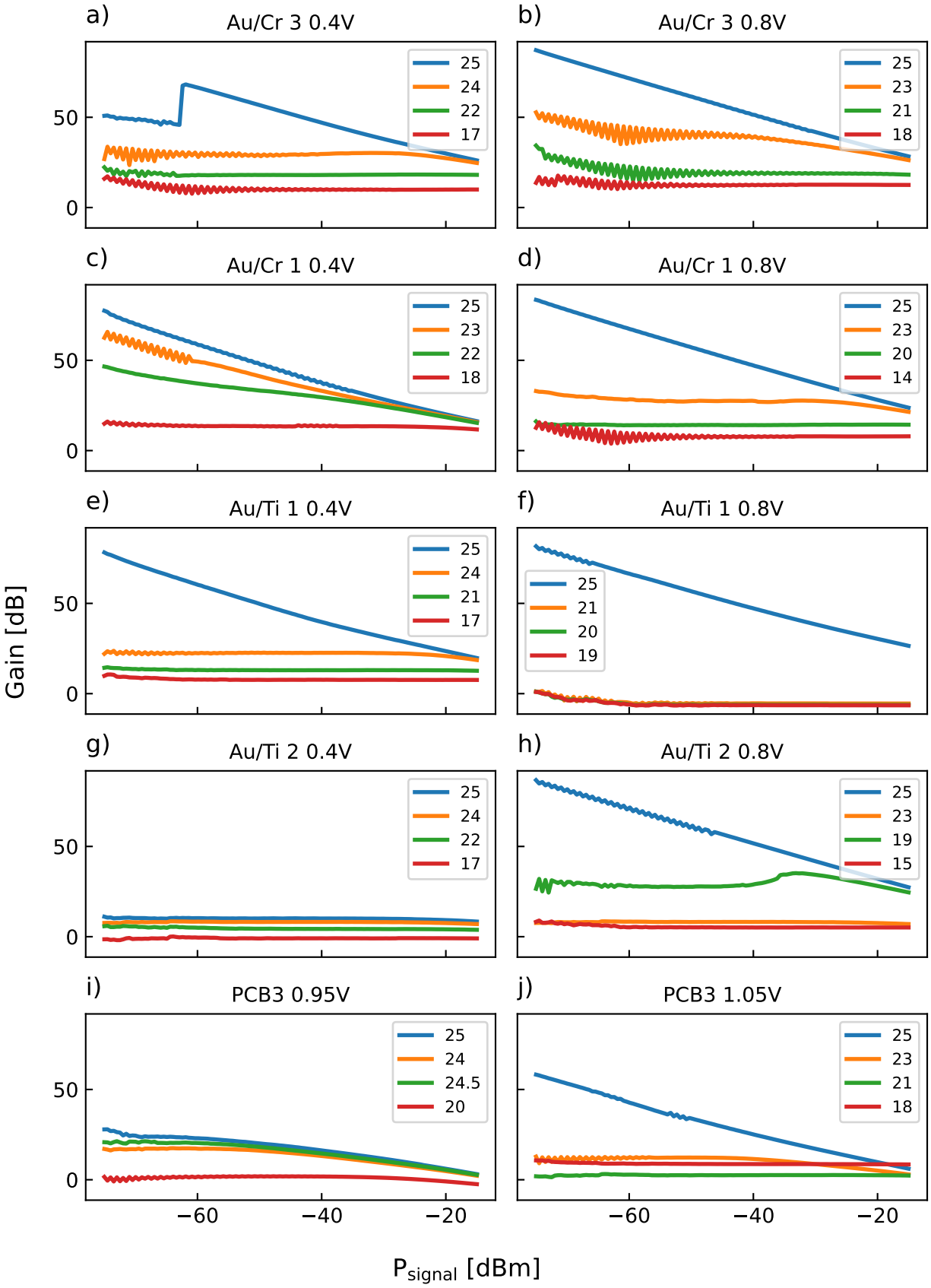

Figure 48: The gain as a function of the input signal power is shown for all working devices. The applied DC bias clearly influences whether the high-gain regime can be reached, but it is not clear what influences the 1 dB compression point or the slope of the pink trace.

6.5 Fabrication Recipe

Spin Coating

1. Clean sample with ITA
2. Place sample on the spin coater (polished face pointing up).
3. Coat sample with LOR-3A (Lift-off resist) using a Pasteur pipette. To avoid bubble formation at all cost.
4. Spin the sample for 50 sec at 4500 rpm with acceleration 1500 rpm/s.
5. Bake sample for 5 min at 180°.
6. Cool sample for 2 min at room temperature.
7. Repeat steps 1. - 4. with positive photoresist S1805.
8. Bake for 2 min at 125°.
9. No cooling necessary, because no additional coating layer added

Laser Writing

1. Place sample in the laser writer and turn on the vacuum.
2. Locate the edge of the sample and translate the design to the coordinates Load design.
3. Use "fast optical" mode or the laser.
4. Set laser power to 10 mW with 42%.
5. Check that the laser is focus on the sample at all times.
6. Expose with laser.

Development

1. Develop in MF319 FOR 64 sec.
2. Rinse in DI for 55 sec
3. Dry with nitrogen

Evaporation

1. Plasma clean the sample for 1 min at 30 W (mashine dependent)
2. Load Ti into evaporator
3. Position sample and open shutter.
4. Evaporate 5 nm of Ti
5. Evaporate 65 nm of Au.

Lift-Off

1. Lift-off with SVC-14 and heatbath at 95°
2. Sonicate at low power for 1 min as last resort, if lift.-off does not work.

Universität Basel

Philosophisch-Naturwissenschaftliche Fakultät

Erklärung zur wissenschaftlichen Redlichkeit und Veröffentlichung der Arbeit (beinhaltet Erklärung zu Plagiat und Betrug)

Titel der Arbeit: Material Dependent Non-linearity and Gain in SrTiO3 Parametric Amplifiers

Name Beurteiler*in: Prof. Dr. Dominik Zumbühl, Dr. Rafael Eggli

Name Student*in: Karthekan Sivasubramaniam

Matrikelnummer: 21-057-443

Mit meiner Unterschrift erkläre ich, dass mir bei der Abfassung dieser Arbeit nur die darin angegebene Hilfe zuteil wurde und dass ich sie nur mit den in der Arbeit angegebenen Hilfsmitteln verfasst habe. Ich habe sämtliche verwendeten Quellen erwähnt und gemäss anerkannten wissenschaftlichen Regeln zitiert.

Ort, Datum: 30.04.2026 Student*in: _____

Wird diese Arbeit veröffentlicht?

○ Nein

● Ja. Mit meiner Unterschrift bestätige ich, dass ich mit einer Veröffentlichung der Arbeit (print/digital) in der Bibliothek, auf der Forschungsdatenbank der Universität Basel und/oder auf dem Dokumentenserver des Departements / des Fachbereichs einverstanden bin. Ebenso bin ich mit dem bibliographischen Nachweis im Katalog SLSP (Swiss Library Service Platform) einverstanden. (nicht Zutreffendes streichen)

Veröffentlichung ab: 01.01.2027

Ort, Datum: 30.04.2026 Student*in: _____

Ort, Datum: _____ Beurteiler*in: _____

Diese Erklärung ist in die Bachelor-, resp. Masterarbeit einzufügen.